

Contents lists available at ScienceDirect

Petroleum Science

journal homepage: www.keaipublishing.com/en/journals/petroleum-science



Original Paper

Response characteristics of shear waves scattered by fractures with borehole observation system



Peng Liu ^a, Hua-Jun Fan ^{b, *}, Meng-Sheng Zhang ^b, Zhen Li ^c, Jing-Wei Jiang ^b, Yuan Gao ^d, Ke-Wen Wang ^a

- ^a PetroChina Research Institute of Petroleum Exploration and Development, Beijing, 100083, China
- b State Key Laboratory of Petroleum Resources and Engineering, China University of Petroleum (Beijing), Beijing, 102249, China
- ^c State Key Laboratory of Oil and Gas Reservoir Geology and Exploitation, Chengdu University of Technology, Chengdu, 610059, Sichuan, China
- ^d Sulige Gas Field Branch, CNPC Greatwall Drilling Company, Panjin, 124010, Liaoning, China

ARTICLE INFO

Article history: Received 18 June 2024 Received in revised form 16 October 2024 Accepted 3 March 2025 Available online 7 March 2025

Edited by Meng-Jiao Zhou and Teng Zhu

Keywords:
Numerical modeling
Wave scattering
Shear wave
Fractures
Borehole observation system

ABSTRACT

Fractures play a crucial role in various fields such as hydrocarbon exploration, groundwater resources management, and earthquake research. The determination of fracture location and the estimation of parameters such as fracture length and dip angle are the focus of geophysical work. In borehole observation system, the short distance between fractures and detectors leads to weak attenuation of elastic wave energy, and high-frequency source makes it easier to identify small-scale fractures. Compared to traditional monopole logging methods, dipole logging method has advantage of exciting pure shear waves sensitive to fractures, so its application is becoming increasingly widespread. However, since the reflected shear waves and scattered shear waves of fractures correspond to different fracture properties, how to distinguish and analyze these two kinds of waves is crucial for accurately characterizing the fracture parameters. To address this issue, numerical simulation of wave responses by a single fracture near a borehole in rock formation is performed, and the generation mechanism and characteristics of shear waves scattered by fractures are investigated. It is found that when the dip angle of the fracture surpasses a critical threshold, the S-wave will propagate to both endpoints of the fracture and generate scattered S-waves, resulting in two distinct scattered wave packets on the received waveform. When the polarization direction of the acoustic source is parallel to the strike of the fracture, the scattered SH-waves always have larger amplitude than the scattered SV-waves regardless of changing the fracture dip angle. Unlike SV-waves, the SH-waves scattered by the fracture do not have any mode conversion. Additionally, propagation of S-waves to a short length fracture can induce dipole mode vibration of the fracture within a wide frequency range. The phenomena of shear waves reflected and scattered by the fracture are further illustrated and verified by two field examples, thus showing the potential of scattered waves for fracture evaluation and characterization with borehole observation system.

© 2025 The Authors. Publishing services by Elsevier B.V. on behalf of KeAi Communications Co. Ltd. This is an open access article under the CC BY-NC-ND license (http://creativecommons.org/licenses/by-nc-nd/4.0/).

1. Introduction

Quantitative prediction of fractures in underground rocks is one of the major challenges in the field of earth science and has important environmental and economical benefits. Although fractures occupy a small volume of subsurface formations, they often dominate fluid flow, transport and rock mechanical deformation.

* Corresponding author. E-mail address: hj.fan@cup.edu.cn (H.-J. Fan). Therefore, fractures play a key role in CO_2 sequestration, hydrogen storage, geothermal energy production and hydrocarbon extraction (Viswanathan et al., 2022). In the observation systems of earth-quake seismology and seismic exploration, the seismic wavelength is usually over 100 m (Wu and Aki, 1985). Fractures or small faults are comparable and even smaller in scale to the seismic wavelength. Moreover, vertical (near-vertical) fractures are more developed than horizontal ones under the overlying formation pressure. As a result, it is difficult to observe the fracture reflection phenomenon in the seismic observation system, while the fracture

scattering phenomenon is more common (Baird et al., 2017; Chen et al., 2019).

Multiple groups of fractures will cause formation heterogeneity when they are randomly distributed or oriented. Aki (1969) analyzed the data collected by ground stations and found that there was a wake signal (coda wave) generated from heterogeneous formation. The coda wave has arrival time lag and longer duration compared with direct wave. As a matter of fact, coda wave represents the scattered wave of small scale structure in heterogeneous formation. The feasibility of evaluating the development of fractures or fracture zones by coda wave has been widely investigated and confirmed (Groenenboom and Falk, 2000; Willis et al., 2006; Burns et al., 2007; Liu and Levander, 2013; Zhu et al., 2015; Guo et al., 2018). The orientation of multiple groups of directional fractures can also be determined by using 3D seismic data (Fang et al., 2014). In natural and artificial earthquake detection, the geophones are usually positioned on the ground. The received scattered waves from underground fractures will be affected by long propagation distance and the loose layer of the surface. The attenuation of scattered waves will increase the difficulty of identifying underground fractures. However, placing geophones in the borehole drilled underground (such as borehole logging technique), can minimize the impact of fracture scattered wave attenuation in signal analyzing (Matsushima et al., 2016; Li et al., 2020).

Many authors have studied the scattered waves of fractures and other geological structures under borehole observation system. Zhao et al. (2022) numerically simulated the acoustic field of borehole scattered waves in formations containing caves, analyzed the mode characteristics of cave scattered waves, and conducted relevant underwater experiments. Hei and Xiao (2019) numerically simulated the dipole shear wave scattering field in heterogeneous formations, pointed out the correlation between the scattered waves attenuation and the heterogeneous objects orientation and verified it by hydraulic fracturing field data. Ben et al. (2020) studied the scattered wavefields measured in two adjacent boreholes and found that the amplitude of scattered P-waves was significantly correlated with the orientation of the scatterer. They proposed that using scattered P-waves to invert the scatterer near the wellbore is highly feasible. Subsequently, Cheng et al. (2023) proposed a specific method for inverting three-dimensional well trajectories using P-waves scattered from adjacent wells. Li et al. (2022) numerically simulated the scattered wave field of the dipole acoustic source in the logging-while-drilling (LWD) of unconsolidated formations, and pointed out that when the target borehole is close to the measurement borehole, the amplitudes of the scattered P-wave and converted wave change significantly with the source distance. Pan et al. (2020) analyzed the reflection and scattering effects based on the synthetic acoustic signals of the real LWD models. They pointed out that the scattering waves by the wellbore bottom are generally much stronger than the reflection signals from the formation layer interfaces. Tang et al. (2016) observed a more pronounced coda wave signal in borehole logging data stimulated by a shear wave source within a hydraulic fractured formation. This coda wave is an S-S scattered wave generated by the densely interconnected artificial fracture network formed through hydraulic fracturing near the borehole. Since the dipole shear wave logging frequency is approximately 4 kHz, the corresponding wavelength is about 1 m. Therefore, the borehole observation system can better evaluate the development of smaller scale fractures compared with seismic observation system. The fracture scale that can be identified by the scattered wave in borehole observation system is from about 0.1 m to 10 m (Wu and Aki, 1988). In this paper, we refer to fractures with a length larger than 10 m as "long length fracture", the length smaller than 10 m as "short length fracture".

The evaluation of formation heterogeneity caused by fracture network system is relatively roughly in previous studies. The accuracy of fracture network image will be significantly improved if every single fracture can be characterized by using scattered waves. Therefore, study of the scattering characteristics of single fracture becomes critical important. Chen et al. (2013) proposed a numerical method that coupled BEM and FDM, and simulated the 2-D scattered wave field generated by a single horizontal fracture (100 m) under the excitation of SH seismic wave (20 Hz). Groenenboom and Falk (2000) recorded the scattered signal of a single hydraulic fracture based on seismic exploration observation system in the laboratory. They pointed out that the elastic wave will have obvious diffraction at the fracture endpoint compared with numerical simulation data. Blum et al. (2011) derived an analytical solution of scattered wave amplitude of a single dry fracture based on linear slip theory, and verified it through ultrasonic experiments. All of these studies are related to numerical simulation or laboratory experiment based on seismic observation system. However, the seismic observation system could only image large-scale fractures or faults with strong scattered wave amplitude. Due to the long wavelength and the large geophone-fracture distance, the seismic method can not clearly image small-scale fractures.

In this paper, we first introduce the theory of S-waves reflected and scattered by a single fracture. Then, we establish a 3D numerical model of a borehole with fractures in a rock formation. Next, we use 3D finite difference algorithm to comprehensively investigate the generation mechanism and response characteristics of SH and SV scattered waves with the borehole observation system. Finally, two field examples are presented to illustrate the difference between the waves received from fractures with long length and short length. The field data processing results are compared with the numerical simulation results. This research is of great significance for better utilizing scattered waves for fracture detection and characterization.

2. Theory and method

2.1. Theory of reflected S-waves by fracture

Suppose there are two sets of orthogonal dipole sources X and Y in the borehole, where the polarization direction of source Y makes an angle φ with respect to the horizontal plane, as illustrated in Fig. 1(a). The S-waves excited by the sources will enter the formation through the borehole, and can be vectorically decomposed into horizontally polarized S-waves (SH) and vertically polarized S-waves (SV). The following relationship can be obtained (Tang and Patterson, 2009; Tang and Wei, 2012):

$$\begin{cases}
X = SHsin \varphi + SVcos \varphi \\
Y = SHcos \varphi + SVsin \varphi
\end{cases}$$
(1)

Assuming there is a fracture above the horizontal borehole, when the angle between the fracture and the borehole observation system is small, the received waveforms are mainly reflected waves (Fig. 1(a)), according to Snell's law. Extensive research results in the field of geophysics, including seismic and logging studies (Shuey, 1985; Tang and Wei, 2012; Zhang et al., 2024), have shown that the SH waves propagating to the fracture will generate SH reflected waves, while the SV waves propagating to the fracture will generate SV reflected waves as well as P reflected waves. Futhermore, these reflected waves will travel down to the borehole and will be received by the two sets of orthogonal dipole receivers X and Y in the borehole. We can thus obtain

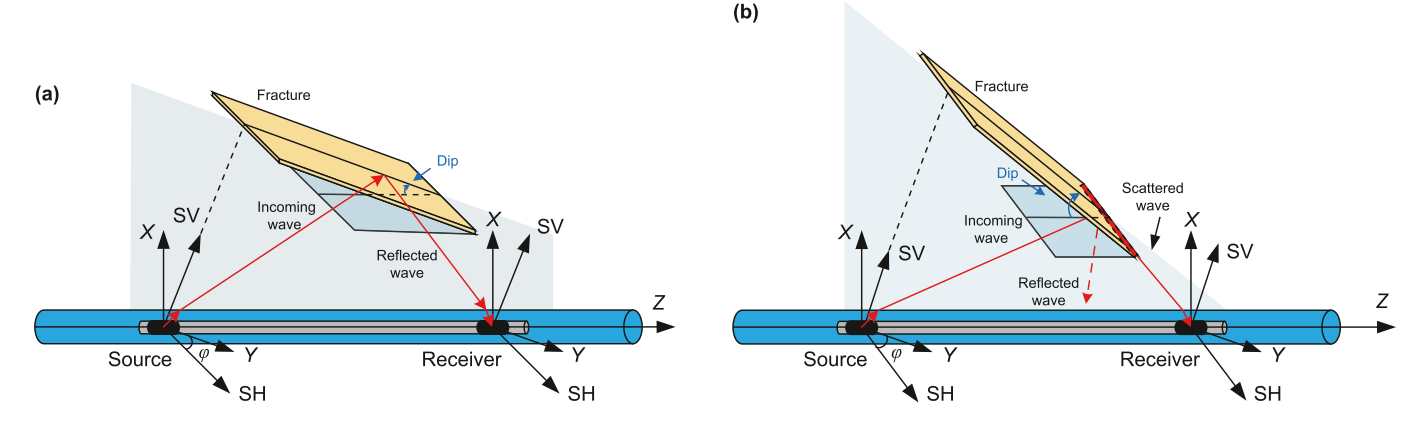


Fig. 1. Schematic diagram of dipole S-wave propagation in a rock formation containing a borehole and a fracture. (a) Reflected wave; (b) scattered wave.

$$\begin{cases} XX = SP\cos^{2} \varphi + SH\sin^{2} \varphi + SV\cos^{2} \varphi \\ YY = SP\sin^{2} \varphi + SH\cos^{2} \varphi + SV\sin^{2} \varphi \\ XY = SP\sin \varphi \cos \varphi - SH\sin \varphi \cos \varphi + SV\sin \varphi \cos \varphi \\ YX = SP\sin \varphi \cos \varphi - SH\sin \varphi \cos \varphi + SV\sin \varphi \cos \varphi \end{cases}$$
(2)

where SP represents the converted reflected P wave which is generated by the incident SV wave on the fracture. The waveform XX represents the waveform that is excited by the X dipole source and received by X receiver. So the four-component receiving waveforms can be obtained: XX, YY, XY, and YX. According to Eq. (2), we know that the received waveforms of four components all comprise converted reflected P waves (SP), pure reflected SH waves, and pure reflected SV waves.

There is a special case that $\varphi = 0^{\circ}$, which happens when the Y source is horizontally polarized and the X source is vertically polarized. Eq. (2) can be simplified as follows:

$$\begin{cases} XX = SP + SV \\ YY = SH \\ XY = 0 \\ YX = 0 \end{cases}$$
 (3)

In this case, the YY waveform only contains pure reflected SH wave. The XX waveform contains reflected SP wave and reflected SV wave. The XY and YX waveforms do not have any signal. During the modeling process in this paper, we take this ideal case and establish a numerical model based on the assumption that φ is 0° .

As the dip angle of the fracture becomes larger, the receiver will not receive the reflected wave signal. Instead, it may receive the scattered wave signal from the endpoint of the fracture (Fig. 1(b)). So in the following content, we will focus on numerical modeling and forward calculation of this situation.

2.2. 3D numerical models

The 3D model comprises a borehole in a rock formation is established (Fig. 2(a)). The length of the calculation area along the vertical axis X, horizontal axis Z, and horizontal axis Y is 8.5 m, 8.5 m, and 4 m, respectively. The elastic parameters of the mediums in the model are shown in Table 1. The borehole axis is coincided with the Z axis, the borehole radius is 0.1 m and it is filled with water. Two orthogonal dipole sources and two orthogonal dipole receivers are placed in the borehole. The receivers are used to obtain four-component dipole waveforms. The source is located at the origin of the coordinates and is spaced 4.92 m from the receiver.

A fracture with short extension is located above the borehole

and is filled with water (Fig. 2(b)). The surface of the fracture extends 4 m along the strike of the fracture (direction of the Y axis), 4 m along the inclination of the fracture (fracture length). The fracture width (thickness) is 20 mm. The vertical distance from the fracture center to the borehole axis is 5 m. A key variable of the fracture is its dip angle θ . When the dip angle is 0° , the fracture is horizontal. For the 90° dip angle, the fracture is vertical. Elastic parameters are shown in Table 1.

2.3. 3D finite difference algorithm

In the forward simulation with borehole observation system, the finite difference method (Leslie and Randall, 1992; Liu et al., 1996; Chen et al., 1998; Liu et al., 2016; Fan et al., 2023) is widely employed. This technique has the advantages for fast computation speed and low memory utilization rate. It serves as a crucial tool to analyze the scattered acoustic field caused by fractures. We use velocity and stress as basic functions to describe the sound field. In an isotropic medium under the Cartesian coordinate system, the equations of motion and constitutive equations described by these two functions are presented as

$$\rho \partial_t v_X = \partial_X \tau_{XX} + \partial_Y \tau_{XY} + \partial_Z \tau_{XZ}
\rho \partial_t v_Y = \partial_X \tau_{XY} + \partial_Y \tau_{YY} + \partial_Z \tau_{YZ} ,
\rho \partial_t v_Z = \partial_X \tau_{XZ} + \partial_Y \tau_{YZ} + \partial_Z \tau_{ZZ}$$
(4)

$$\frac{\partial \tau_{xx}}{\partial t} = (\lambda + 2\mu) \frac{\partial v_x}{\partial x} + \lambda \frac{\partial v_y}{\partial y} + \lambda \frac{\partial v_z}{\partial z} + g_{xx}
\frac{\partial \tau_{yy}}{\partial t} = \lambda \frac{\partial v_x}{\partial x} + (\lambda + 2\mu) \frac{\partial v_y}{\partial y} + \lambda \frac{\partial v_z}{\partial z} + g_{yy}
\frac{\partial \tau_{zz}}{\partial t} = \lambda \frac{\partial v_x}{\partial x} + \lambda \frac{\partial v_y}{\partial y} + (\lambda + 2\mu) \frac{\partial v_z}{\partial z} + g_{zz}
\frac{\partial \tau_{yz}}{\partial t} = \mu \left(\frac{\partial v_y}{\partial z} + \frac{\partial v_z}{\partial y} \right)
\frac{\partial \tau_{xz}}{\partial t} = \mu \left(\frac{\partial v_x}{\partial z} + \frac{\partial v_z}{\partial x} \right)
\frac{\partial \tau_{xy}}{\partial t} = \mu \left(\frac{\partial v_x}{\partial y} + \frac{\partial v_z}{\partial x} \right)$$
(5)

where v_X , v_Y and v_Z are particle vibration velocity components in the x, y and z directions respectively; τ_{XX} , τ_{yy} and τ_{ZZ} are the normal stresses in the x, y and z directions respectively; τ_{XY} , τ_{XZ} , τ_{YZ} are shear stresses; ρ is the density of the medium; λ , μ are Lame coefficients of the medium. g_{XX} , g_{YY} , g_{ZZ} are stress source. The stress

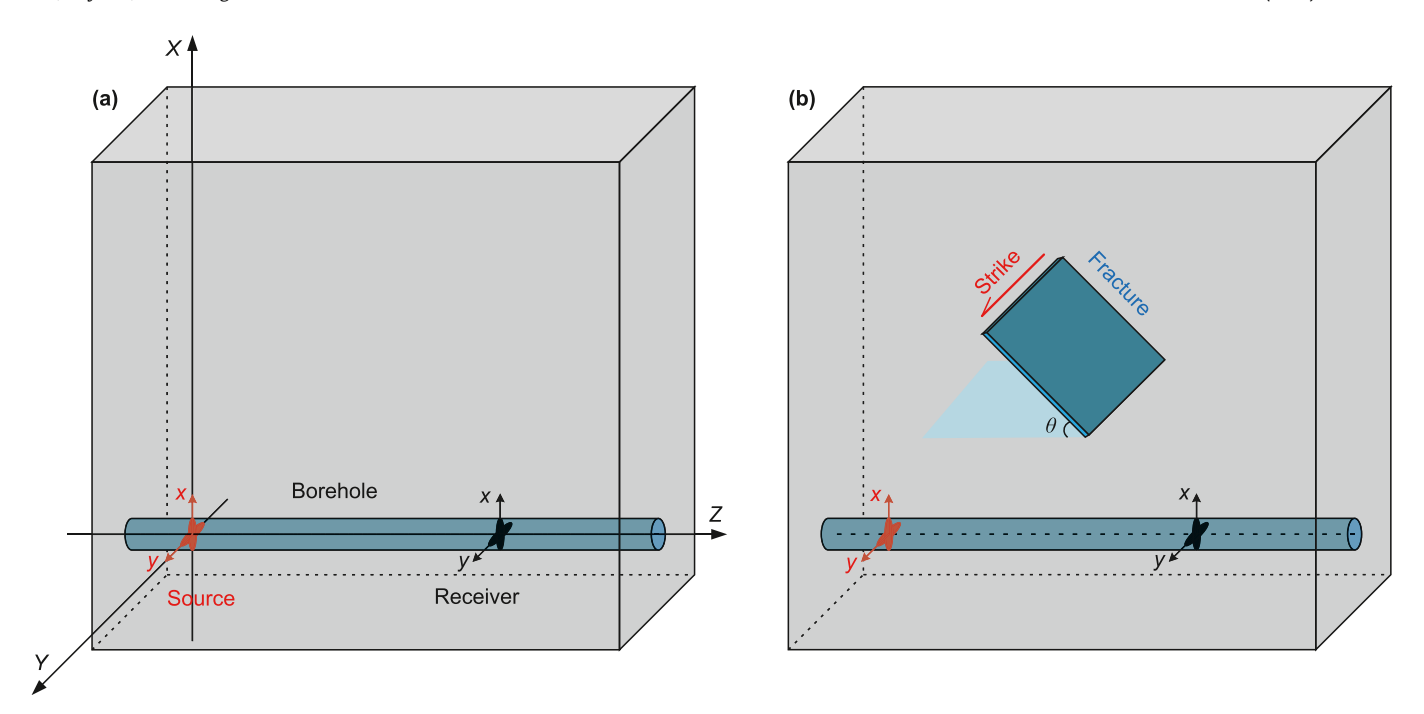


Fig. 2. Schematic diagram of a borehole in a rock formation. (a) Without fracture; (b) with short extension fracture.

 Table 1

 Elastic parameters of mediums for finite difference simulation.

Media	ν _p , km/s	ν _s , km/s	ρ, g/cm ³
Rock formation	3.810	2.540	2.500
Water	1.500	_	1.000

source loaded by two point sources (very close together, with the same amplitude but opposite phase) excited. The source function in this paper is narrow-band source and can be described as

$$v_{x}^{n+1/2} = v_{x}^{n-1/2} + \frac{\Delta t}{\rho} \left(D_{x} \tau_{xx}^{n} + D_{y} \tau_{xy}^{n} + D_{z} \tau_{xz}^{n} + f_{x}^{n} \right)$$

$$v_{y}^{n+1/2} = v_{y}^{n-1/2} + \frac{\Delta t}{\rho} \left(D_{x} \tau_{xy}^{n} + D_{y} \tau_{yy}^{n} + D_{z} \tau_{yz}^{n} + f_{y}^{n} \right),$$

$$v_{z}^{n+1/2} = v_{z}^{n-1/2} + \frac{\Delta t}{\rho} \left(D_{x} \tau_{xz}^{n} + D_{y} \tau_{yz}^{n} + D_{z} \tau_{zz}^{n} + f_{z}^{n} \right)$$

$$(7)$$

$$S(t) = \begin{cases} \frac{1}{2} \left[1 + \cos\left(\frac{2\pi}{T_c} \left(t - t_0 - \frac{T_c}{2} \right) \right) \right] \cos\left(2\pi f_0 \left(t - t_0 - \frac{T_c}{2} \right) \right), & t_0 \le t \le T_c + t_0 \\ 0, & t < t_0, & t > T_c + t_0 \end{cases}$$
 (6)

The dominant frequency of the source f_0 is 3500 Hz, the time width of the source function $T_{\rm c}$ is 0.001 s, and the delay time of the source t_0 is 0.0005 s.

Then the staggered grid is used to discretize the wave Eqs. (4) and (5). As shown in Fig. 3, the normal stress τ_{xx} , τ_{yy} , τ_{zz} are in the center of the grid element with their spatial coordinates defined as $(i\Delta x, j\Delta y, k\Delta z)$. The sampling time is $n\Delta t$. The parameters i, j, k, n are integers. The parameters $\Delta x, \Delta y, \Delta z$ represent spatial sampling intervals and Δt represents the time sampling interval. We set $\Delta x = \Delta y = \Delta z = 10$ mm in the model. The normal stress can be denoted as $\tau_{xx}^n(i, j, k)$, $\tau_{yy}^n(i, j, k)$ and $\tau_{zz}^n(i, j, k)$. On this basis, second order difference format is adopted in time, and Eqs. (4) and (5) are approximated as

$$\begin{split} &\tau_{xx}^{n+1} = \tau_{xx}^{n} + \Delta t \left\{ (\lambda + 2\mu) D_{x} v_{x}^{n+1/2} + \lambda D_{y} v_{y}^{n+1/2} + \lambda D_{z} v_{z}^{n+1/2} + g_{xx}^{n+1/2} \right\} \\ &\tau_{yy}^{n+1} = \tau_{yy}^{n} + \Delta t \left\{ \lambda D_{x} v_{x}^{n+1/2} + (\lambda + 2\mu) D_{y} v_{y}^{n+1/2} + \lambda D_{z} v_{z}^{n+1/2} + g_{yy}^{n+1/2} \right\} \\ &\tau_{zz}^{n+1} = \tau_{zz}^{n} + \Delta t \left\{ \lambda D_{x} v_{x}^{n+1/2} + \lambda D_{y} v_{y}^{n+1/2} + (\lambda + 2\mu) D_{z} v_{z}^{n+1/2} + g_{zz}^{n+1/2} \right\} \\ &\tau_{yz}^{n+1} = \tau_{yz}^{n} + \lambda \Delta t \left(D_{z} v_{x}^{n+1/2} + D_{y} v_{z}^{n+1/2} + g_{yz}^{n+1/2} \right) \\ &\tau_{xz}^{n+1} = \tau_{xz}^{n} + \lambda \Delta t \left(D_{z} v_{x}^{n+1/2} + D_{x} v_{z}^{n+1/2} + g_{xz}^{n+1/2} \right) \\ &\tau_{xy}^{n+1} = \tau_{xy}^{n} + \lambda \Delta t \left(D_{y} v_{x}^{n+1/2} + D_{x} v_{y}^{n+1/2} + g_{xy}^{n+1/2} \right) \end{split} \tag{8}$$

where $D_h \tau_{pq}$ and $D_h v_p$ is the central difference approximation of the stress and velocity component in the h direction, respectively. The

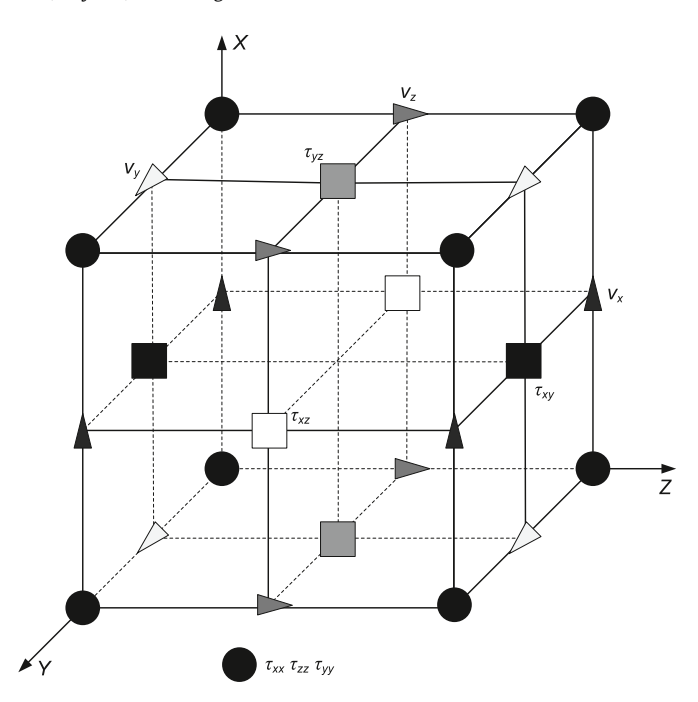


Fig. 3. Schematic diagram of finite difference staggered grid.

parameters h, p and q can be x, y and z. The specific form of its 2n order precision is written as

$$D_{h}\tau_{pq} = \frac{1}{\Delta h} \sum_{m=0}^{n-1} a_{m} \left[\tau_{pq} \left(h + \frac{2m+1}{2} \Delta h \right) - \tau_{pq} \left(h - \frac{2m+1}{2} \Delta h \right) \right],$$

$$D_{h}v_{p} = \frac{1}{\Delta h} \sum_{m=0}^{n-1} a_{m} \left[v_{p} \left(h + \frac{2m+1}{2} \Delta h \right) - v_{p} \left(h - \frac{2m+1}{2} \Delta h \right) \right]$$
(9)

with a_m the difference approximation coefficient. To ensure a stable simulation outcome, we impose constraints on the time sampling interval:

$$\Delta t \le \frac{\Delta h}{v_{\text{max}}} \sqrt{3} \sum_{m=0}^{n-1} a_m, \tag{10}$$

where ν_{max} is the largest velocity in all mediums in the model, Δh is the smallest space step, and 2n is the order of difference approximation. In addition, in order to eliminate the false reflection caused by artificial truncation, artificial absorption boundary should be added to the periphery of the model (Collino and Tsogka, 2001; Wang and Tang, 2003). We employ the method of complex frequency shifted perfectly matched layer (CFS-PML).

In the numerical models, the fluid-solid coupling is mainly involved in two places: one is the borehole wall and the other is the fracture interface. The boundary conditions of continuous normal velocity, equal normal stress in the solid and negative acoustic pressure in the fluid, and zero tangential stress should be satisfied at the fluid-solid interface, to proceed the finite difference acoustic field calculation at the boundary of fluid-solid (as shown in Eq. (10)). To address this issue, the lowest second-order finite difference is used to reduce the influence of adjacent grids. Moreover, the tangential stress and tangential strain on the fluid side is fixed at 0 as the absence of shear stress and shear strain in fluid.

To verify the reliability of finite difference method, the received waveforms are also calculated and compared by using the real-axis

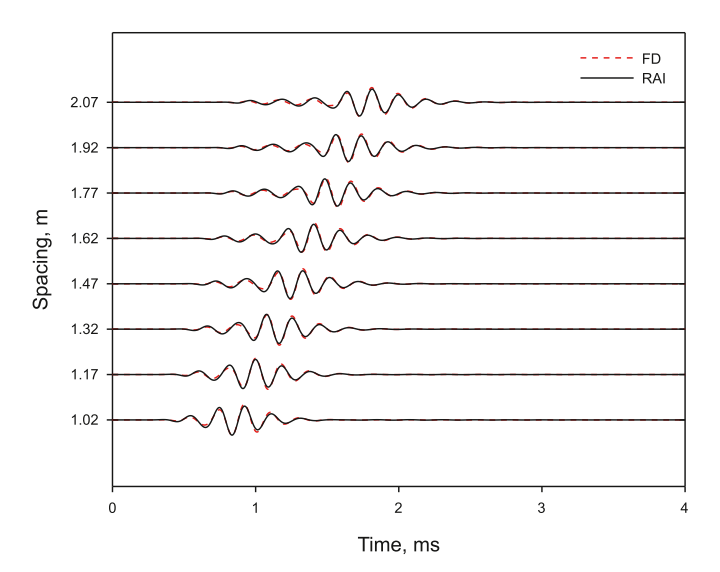


Fig. 4. Comparison of waveforms calculated by using finite difference (FD) and real-axis integration (RAI) methods.

integration method. The model for calculation contains an isotropic formation and one horizontal borehole. The parameters are from Table 1, and the sound source is a dipole source. The waveforms calculated by the real-axis integration method and the finite difference method are essentially consistent (Fig. 4). The results confirm the accuracy of the finite difference algorithm used in this paper.

3. Fracture scattering mechanism

In Section 2.2, we established two formation models. For the first model, there is a borehole in the formation (Fig. 2(a)). For the second model, besides the borehole, there is also a fracture with short length in the formation (Fig. 2(b)). We use 3D finite difference method to carry out forward simulation of these two models, and then obtain the dipole S-wave waveforms under the two models. The received waveform related to the model in Fig. 2(a) only contains the direct wave signal propagating along the borehole. However, the waveform of the model in Fig. 2(b) contains both the direct waves, and the reflected or scattered waves from the fracture near the borehole. Therefore, by subtracting the direct wave of Fig. 2(a), the reflected or scattered waveforms of the fracture of Fig. 2(b) can be obtained.

After removing the direct wave in the borehole, we obtain the received waveforms from the fracture with different dip angle (Fig. 5). The waveforms are excited by horizontally polarized source and received by horizontally polarized receiver (YY waveform). When the fracture dip angle is 20° or less, there is only one wave packet in the waveform with strong amplitude. The arrival time of the head wave in the waveforms of 0°, 10° and 20° dip angles are all about 4.8 ms. By calculating the sound propagation path, it is found that the wave is pure reflected SH-SH wave. When the fracture dip angle is larger than 20°, the wave amplitude decreases sharply and it splits into two wave packets. According to Snell's law, the receiver can only receive scattered wave instead of reflected wave when the fracture dip angle is large. The first wave packet should be the scattered wave corresponding to the near-end of the fracture close to the borehole, while the second one should be related to the farend of the fracture. With the increase of the dip angle, the arrival time of the near-end scattered waves becomes earlier because it is closer to the borehole. By contrast, the far-end scattered waves

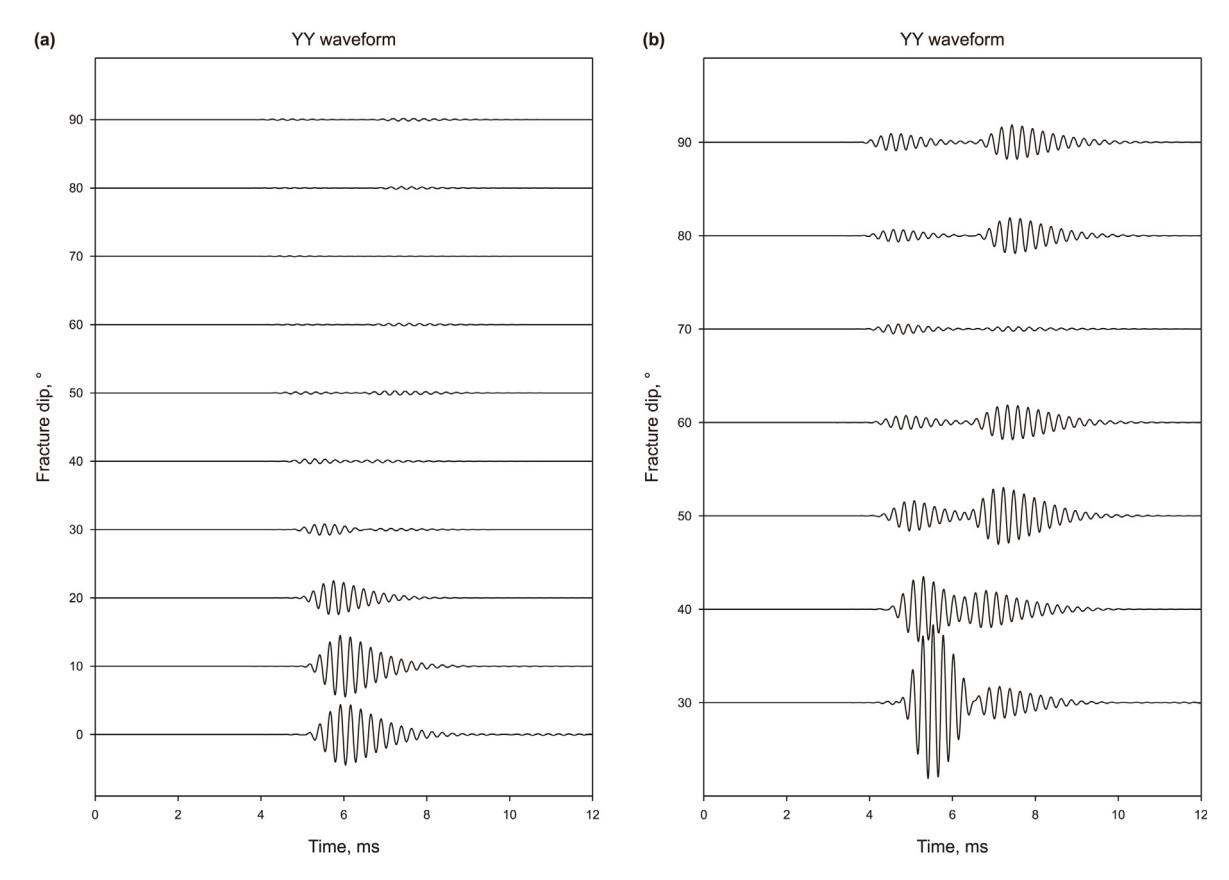


Fig. 5. The received waveforms from fractures with different dip angles. It is the horizontally polarized source excitation, and the horizontally polarized receiver receiving waveform (YY). The direct wave signal is removed from the waveform. (a) Received waveforms with fracture dip angles from 0° to 90° ; (b) tenfold-amplified waveforms with fracture dip angles from 30° to 90° .

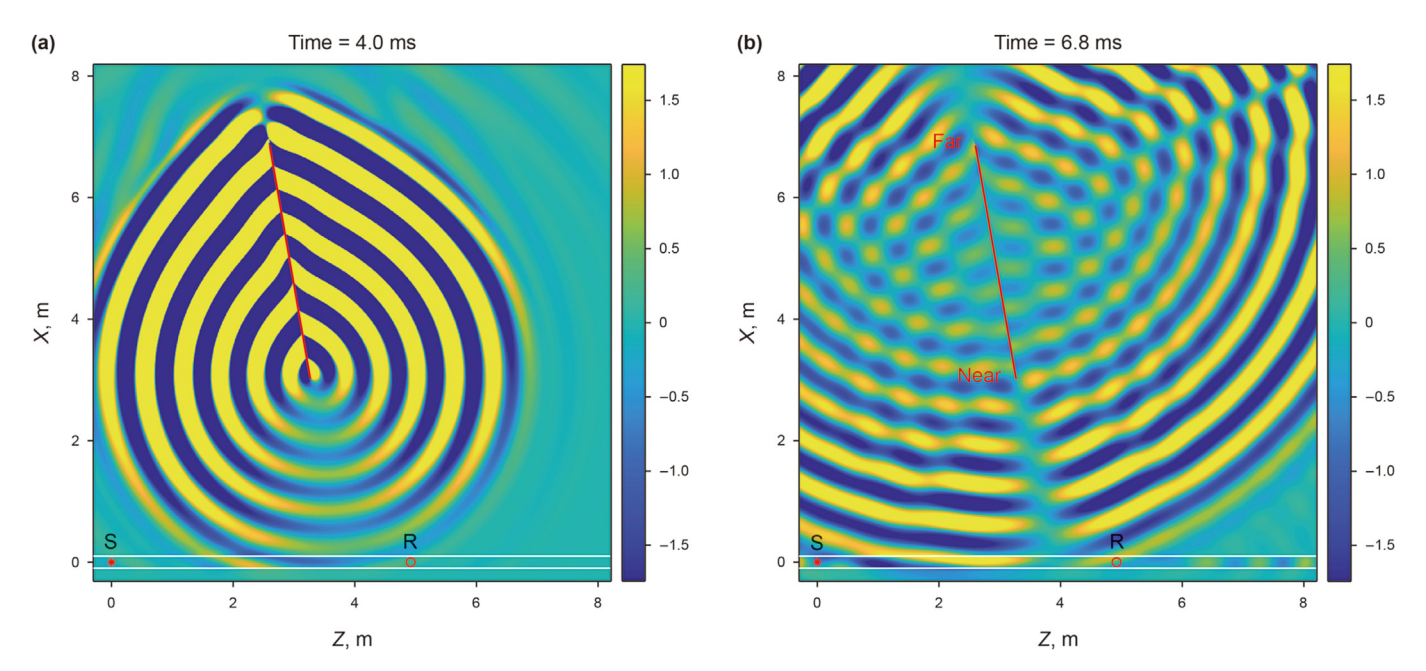


Fig. 6. The snapshot of the XOZ plane sound field excited by horizontally polarized source and received by horizontally polarized receiver. The fracture has the dip angle 80°, width 20 mm, length 4 m. The solid red line represents the short-length fracture. **(a)** 4.0 ms sound field slice; **(b)** 6.8 ms sound field slice.

arrive later when the fracture dip angle increases. The angle increase leads to a more distinct separation between the two scattered waves. When the dip angle reaches 80° , the arrival time of the near-end scattered wave is 4.0 ms and that of the far-end scattered wave is 6.8 ms.

To further investigate the scattered waves, snapshots of the sound fields excited by horizontally polarized source and received by horizontally polarized receiver in the model containing a 80° fracture is presented in Fig. 6. The direct waves have been removed. In the borehole, the source (S) is on the left and the receiver (R) is 4.92 m right from the source. In Fig. 6(a), the time is 4.0 ms. We can see that the scattered wave signal is generated at the near-end point of the fracture. The scattered wave propagates downwards, and the wave front reaches the receiver (R) at the time 4.0 ms, which indicates that the head wave of YY waveform in Fig. 5 is indeed the scattered wave at the near-end of the fracture. In addition, the scattered waves propagate upwards along the edge of the fracture. Interestingly, the scattered waves on both sides of the fracture vibrate inversely, which is related to the vibration modes of the fracture itself. We will discuss this phenomenon further in Section 4.2. In Fig. 6(b), the time is 6.8 ms. We can also observe that the wavefront is now just reaching the receiver, which is the corresponding scattered wave at the far-end of the fracture. This result is also consistent with that presented in Fig. 5.

The waveforms excited by vertically polarized sound source and received by vertically polarized receiver (XX waveform) are plotted in Fig. 7. When the dip angle of the fracture is 20° or less, the waveform amplitude is strong. The arrival time of the head wave is

about 3.6 ms, which is earlier than that in the YY waveform (4.8 ms, Fig. 5). The reason is that, the SV wave generated by the vertically polarized source undergoes mode conversion upon encountering the fracture, resulting in a reflected SV-P wave which has earlier arrival time. When the fracture dip angle is greater than 20°, the amplitude of the received waveform decreases significantly. The waveform also begins to split into two wave packets as the dip angle increases. They are also related to scattered waves at the near and far endpoints of the fracture, respectively. When the dip angle reaches 80°, the arrival time of the near-end scattered wave is 3.2 ms, which is obviously earlier than that of the YY waveform (4.0 ms, Fig. 5).

To further analyze the scattered wave generated by SV shear wave, we also present snapshots of the sound fields stimulated by vertically polarized source and received by vertically polarized receiver in the model containing a 80° fracture (see Fig. 8). In Fig. 8(a), the time is 3.2 ms, the scattered wavefront generated by the near-end of the fracture just reaches the receiver. This phenomenon indicates that the head wave in XX waveform is indeed the scattered wave at the near-end of the fracture, which is the SV-P scattered wave. Because of the SV-P and SV-SV waves, the SV scattered waves propagating upward along the edge of fracture exhibits weaker symmetry (Fig. 8(a)) compared with the SH scattered waves (Fig. 6(a)). In Fig. 8(b), the time is 6.8 ms. The far and near endpoints of the fracture act as secondary sources, and the excited scattered waves propagate outwards. The wavefront of the far-end scattered wave in Fig. 8(b) has propagated to a position below the borehole, whereas that in Fig. 6(b) remains above. So it can be inferred that, the far-end scattered wave excited by a

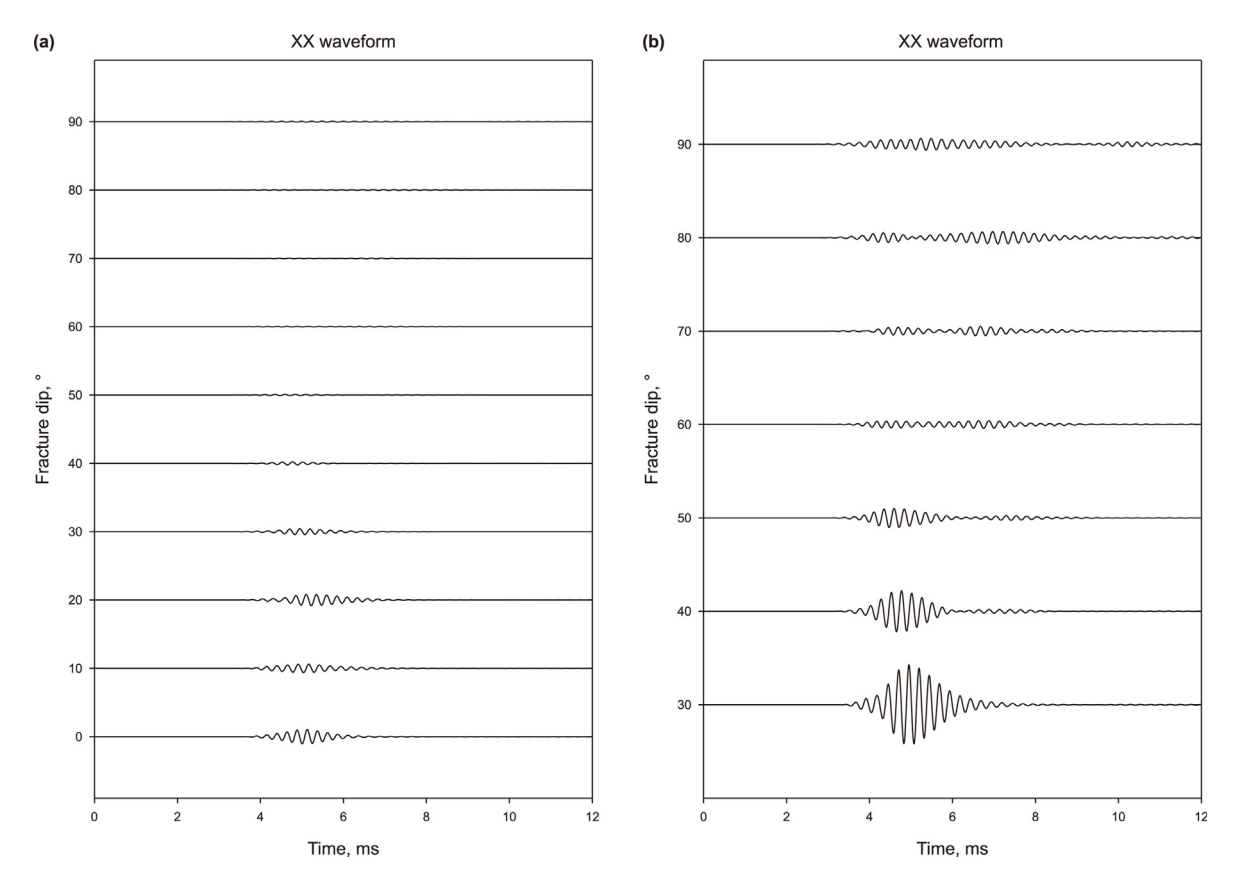


Fig. 7. The received waveforms from fractures with different dip angles. It is the vertically polarized source excitation, and the vertically polarized receiver receiving waveform (XX). The direct wave signal is removed from the waveform. (a) Received waveforms with fracture dip angles from 0° to 90°; (b) tenfold-amplified waveforms with fracture dip angles from 30° to 90°.

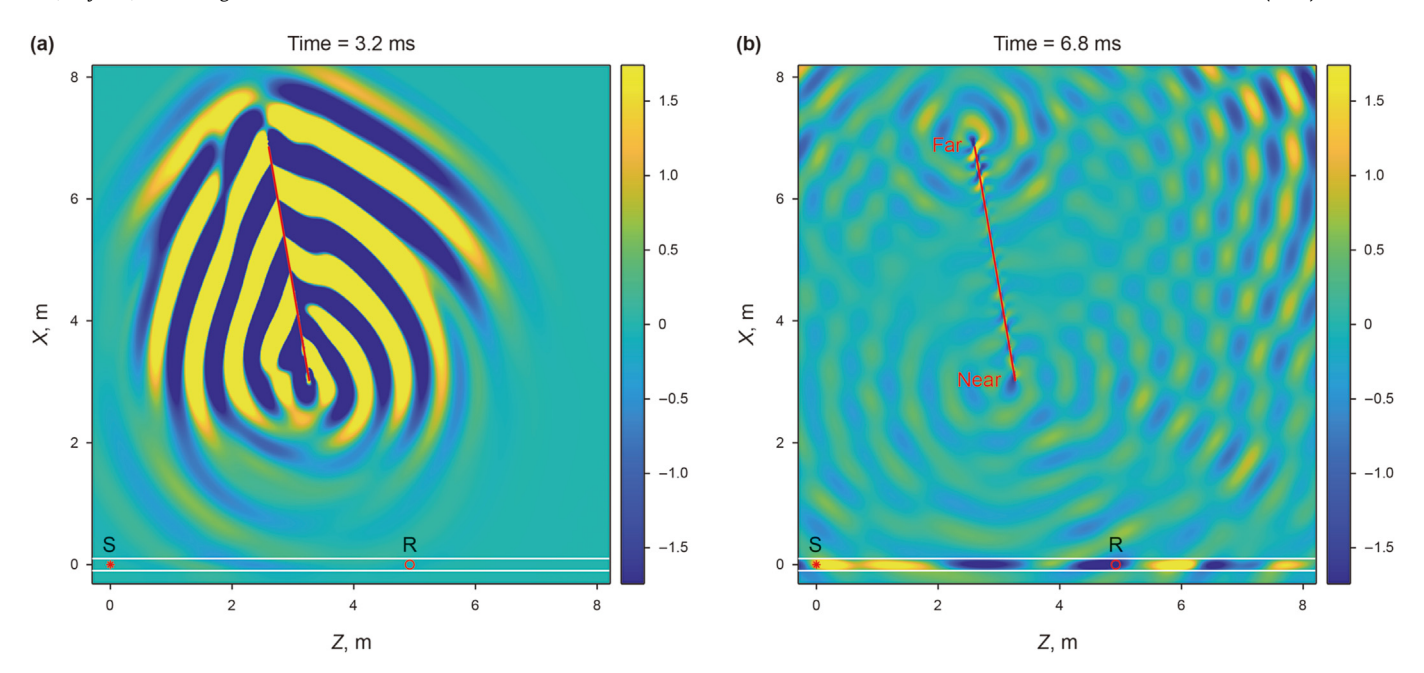


Fig. 8. The snapshot of the XOZ plane sound field excited by vertically polarized source and received by vertically polarized receiver. The fracture has the dip angle 80°, width 20 mm, length 4 m. (a) 3.2 ms sound field slice; (b) 6.8 ms sound field slice.

vertically polarized source arrives at the receiver earlier than that excited by a horizontally polarized source.

The comparison of the waveforms of YY (Fig. 5) and XX (Fig. 7) reveals that, for the model of Fig. 2(b), the amplitude of SV scattered wave is always weaker than that of SH scattered wave, no matter how the fracture dip angle changes. This phenomenon is also clearly shown in the sound fields (Figs. 6 and 8), which indicates that the SH wave is more prone to fracture scattering than SV wave. In practical situations, we should pay more attention to the

detection and extraction of SH wave scattered signal.

4. Fracture scattered wave analysis

In this section, we conduct systematic study on the scattered wave of fracture with short length near a borehole using the model of Fig. 2(b), with the purpose of identifying several scattering characteristics of fractures.

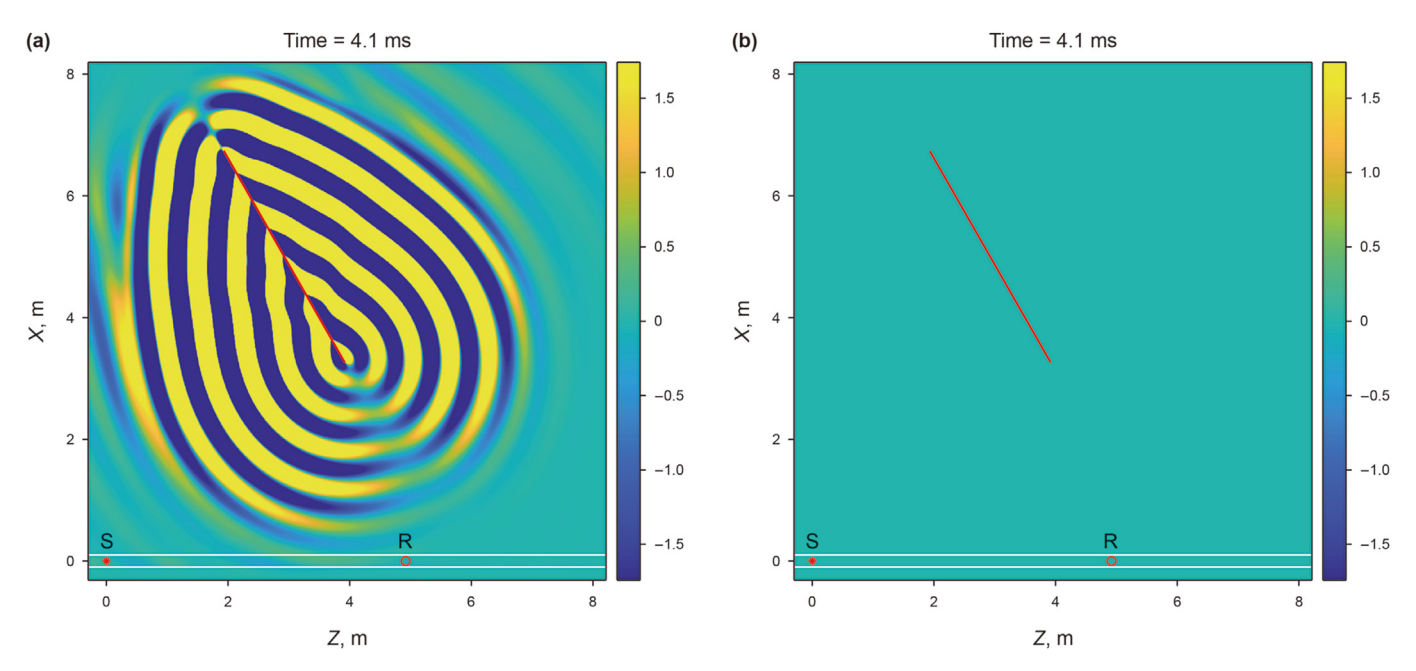


Fig. 9. The snapshot of the XOZ plane sound field excited by a horizontally polarized source. The time is 4.1 ms, the dip angle of the fracture is 60°, the width is 20 mm, and the length is 4 m. (a) Vy component sound field slice; (b) Vx component sound field slice.

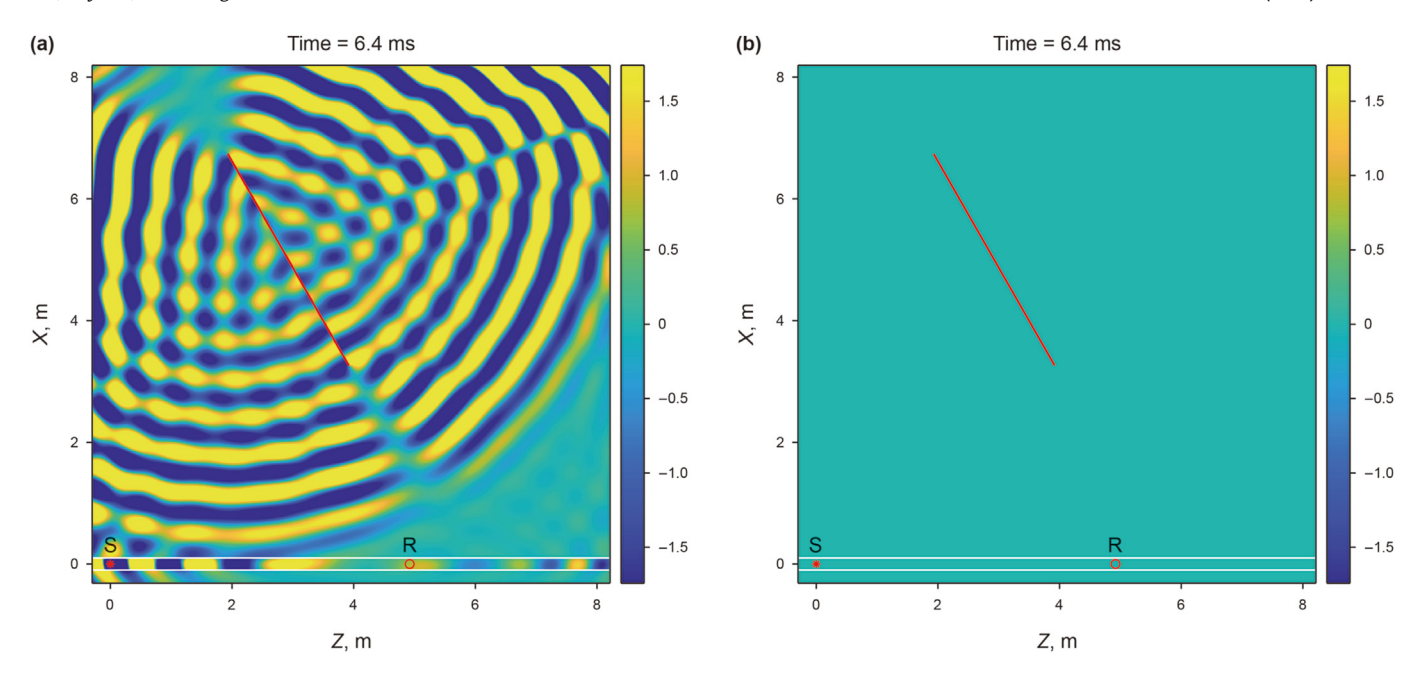


Fig. 10. The snapshot of the XOZ plane sound field excited by a horizontally polarized source. The time is 6.4 ms, the dip angle of the fracture is 60°, the width is 20 mm, and the length is 4 m. (a) Vy component sound field slice; (b) Vx component sound field slice.

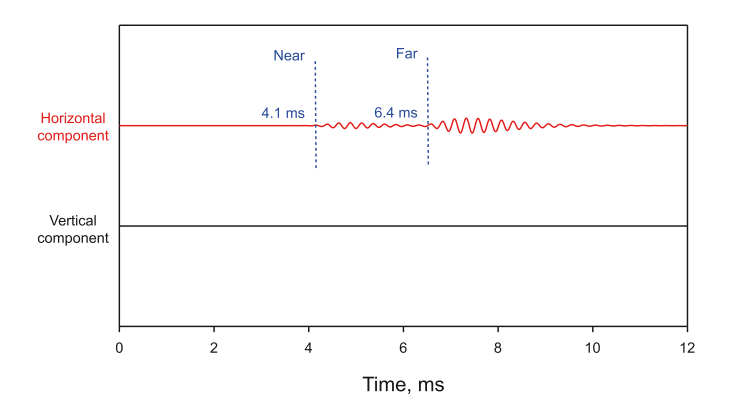


Fig. 11. The received waveforms of receivers with different polarization directions excited by a horizontally polarized source. The fracture has a dip angle of 60° , a width of 20 mm and a length of 4 m. The solid red line represents the waveform that is received by horizontally polarized receiver. The black solid line represents the waveform that is received by vertically polarized receiver.

4.1. Mode characteristics of fracture scattered waves

It should be noted that the dip angle of the fracture is fixed at 60° in this section. The forward modeling results of this model indicate that at the near-end of the fracture, the scattered wave only exists in the sound field excited by horizontally polarized source and received by horizontally polarized receiver (*Vy* component) (Fig. 9(a)). More importantly, there is no energy in the sound field excited by horizontally polarized source and received by vertically polarized receiver (*Vx* component) (Fig. 9(b)). Upon reaching the near-end of a short length fracture, the SH wave only generates scattered SH wave without any mode conversion to scattered SV or scattered P wave. This phenomenon of scattered SH wave is consistent with the characteristic that reflected SH wave does not have the mode conversion. The scattered sound field at the

far-end of the fracture is similar with the near-end of the fracture. The scattered wave is only presented in the Vy component sound field, and there is no energy in the Vx component sound field (Fig. 10). To compare the results with the sound fields, the waveforms are presented in Fig. 11. Two scattered wave packets are generated from the two endpoints of the fracture in the Vy component waveform, which are consistence with the sound field results (Figs. 9 and 10). The energy remains zero in the Vx component waveform. We can conclude that, for the model of Fig. 2(b), the SH wave will become pure scattered SH-SH wave when it propagates to the endpoints of the fracture, without mode conversion.

4.2. Radiation characteristics of fracture scattered waves

In Section 3, we have mentioned the phenomenon of inverse vibration of scattered waves on both sides of a fracture. We will discuss this phenomenon further in this section. Snapshots of sound fields excited by horizontally polarized source and received by horizontally polarized receiver in the model containing a 90° fracture is presented in Fig. 12. The scattered waves from the nearend of the fracture arrive at the receiver by 4.0 ms (Fig. 12(a)). We find that a portion of the scattered wave propagates downwards and is received by the receiver in the borehole. Other part of the scattered energy travels upwards along the edge of the fracture, causing the fluid-filled fracture to vibrate in dipole mode. The vibration mode of the fracture is antisymmetric mode, which is similar to a dipole source. And the scattered wave energy of antisymmetric mode will be radiated into the formation. The polarity of the sound field on both sides of the fracture is opposite. At 6.8 ms, the scattered waves from the far-end of the fracture are approaching the receiver (Fig. 12(b)). The scattered wave propagates downwards along the edge of the fracture. Similar with the near-end, the fracture is also subjected to antisymmetric mode vibration. As a consequence, the sound field on both sides of the

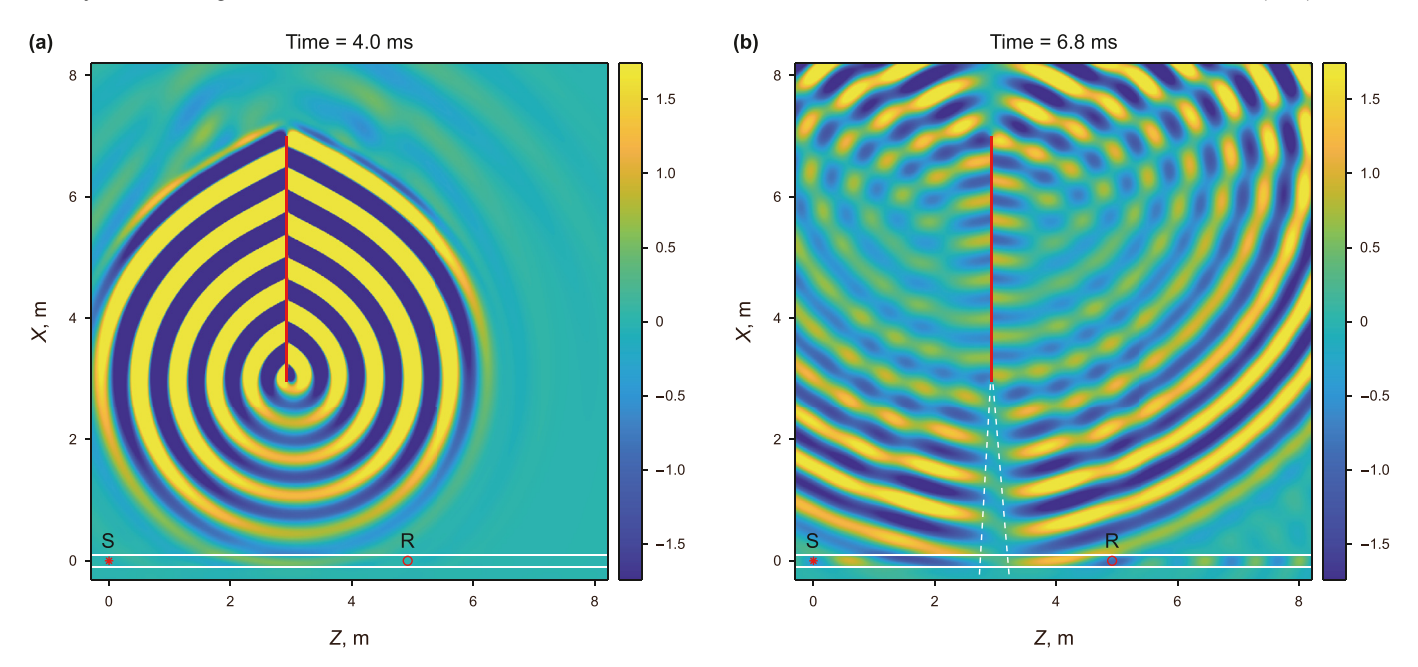


Fig. 12. The snapshot of the XOZ plane sound field excited by horizontally polarized source and received by horizontally polarized receiver. The fracture has a dip angle of 90°, a width of 20 mm and a length of 4 m. **(a)** 4.0 ms sound field slice; **(b)** 6.8 ms sound field slice.

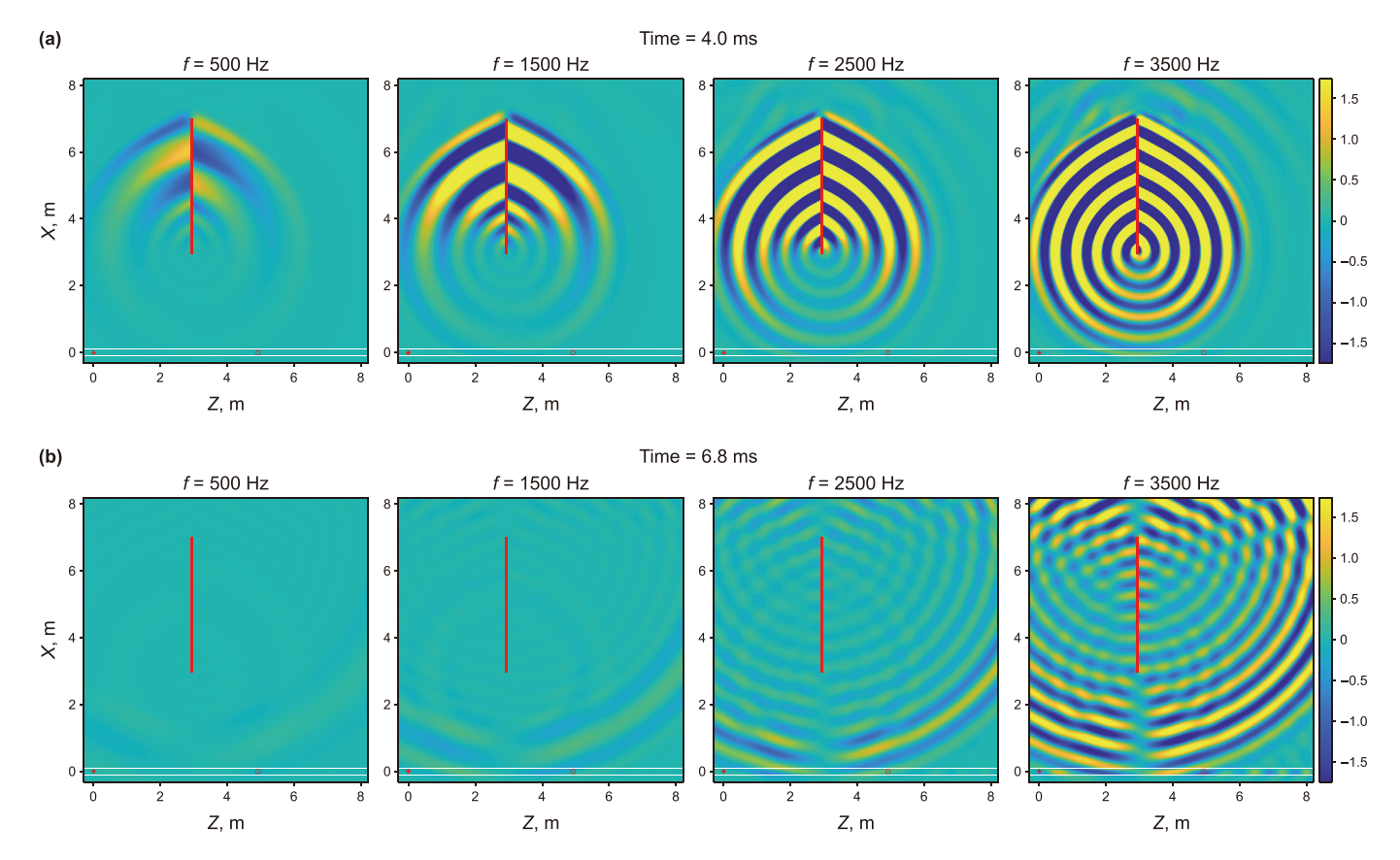


Fig. 13. The snapshot of the XOZ plane sound field excited by horizontally polarized source with different frequencies (f), and received by horizontally polarized receiver. The fracture has a dip angle of 90°, a width of 20 mm and a length of 4 m. (a) 4.0 ms sound field slice; (b) 6.8 ms sound field slice.

fracture has the reversed polarity. As the two types of inverting scattered waves continue to propagate downwards from near-end of the fracture, the interference will happen. Consequently, the two waves are eliminated due to the absence of the fractures, which generates a region with minimal sound field energy (the area between two white dotted lines in Fig. 12(b)).

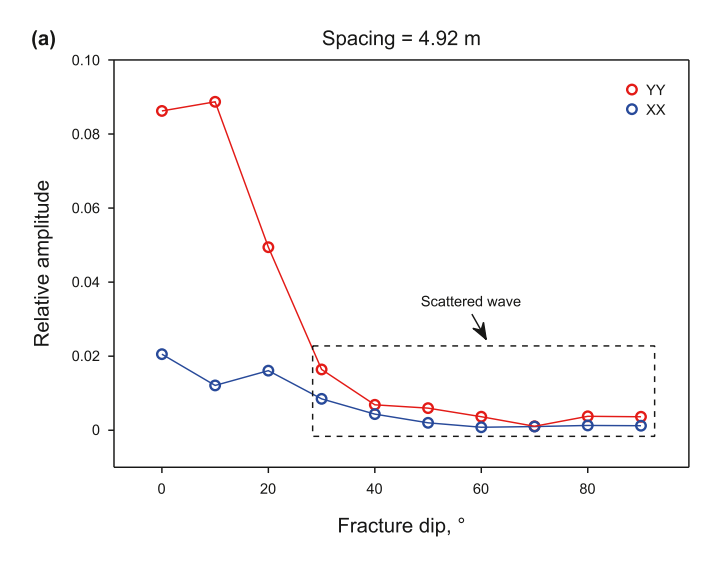
On this basis, we also computed the scattered wave field excited by sound sources with different frequencies (see Fig. 13). We found that when the source frequency decreases, the wavelength of the scattered wave becomes larger, and the scattered wave energy decreases significantly. However, the sound field on both sides of the fracture remains the reversed polarity. This phenomenon demonstrates that the radiation characteristics of fracture scattered waves proposed in this section are applicable within a wide frequency range.

4.3. Amplitude characteristics of fracture scattered waves

The scattered wave amplitude in YY waveform is stronger than that in XX waveform, no matter how the dip angle of the fracture changes (compare Figs. 5 and 7). According to the model of the rock formation with a borehole (Fig. 2(a)), the waveforms of XX and YY are the same. The direct wave amplitudes $A_{\rm D}$ is defined as

$$A_{\rm D} = \frac{\int_{t_{\rm B}}^{t_{\rm E}} |W(t)| dt}{t_{\rm F} - t_{\rm B}},\tag{11}$$

where W(t) represents shear wave amplitude at time t, $t_{\rm B}$ represents the start time of calculation, and $t_{\rm E}$ represents the end time of calculation. Since there is only pure direct S-wave in the waveform, $t_{\rm B}$ can be 0, and $t_{\rm E}$ can be the maximum recording time of 12 ms. The received waveform in the model without the fracture (Fig. 2(a)) is subtracted from the waveform in the model containing a fracture with short length (Fig. 2(b)), thus eliminating the effect of direct waves. Eq. (11) can be used to calculate the scattered wave amplitudes of XX component $A_{\rm SXX}$ and YY component $A_{\rm SYY}$. Additionally, we put forward the concept of relative amplitude as



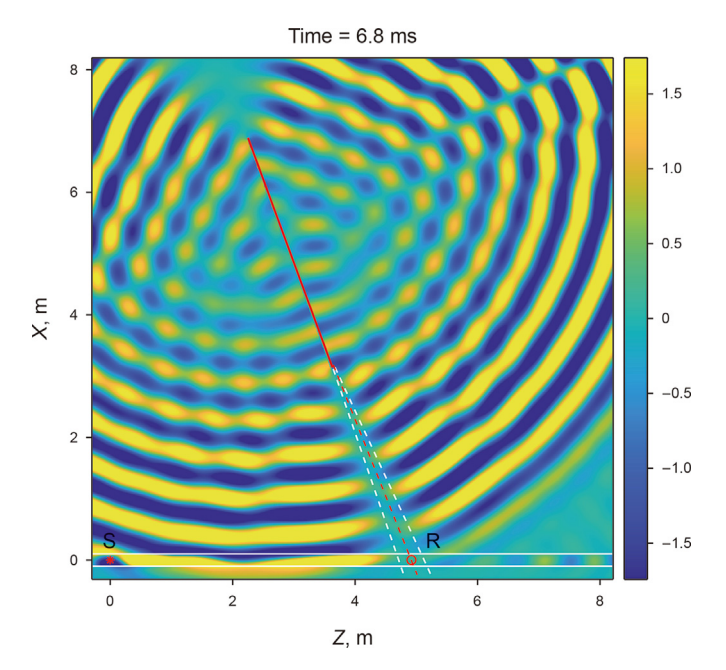


Fig. 15. The snapshot of the XOZ plane Vy component sound field excited by a horizontally polarized source. The time is 6.8 ms, the dip angle of the fracture is 70° , the width is 20 mm, and the length is 4 m.

$$\begin{cases}
RA_{SXX} = A_{SXX}/A_{D} \\
RA_{SYY} = A_{SYY}/A_{D}
\end{cases}$$
(12)

where *RA*_{SYY} represents the relative amplitude of YY component scattered waves, and *RA*_{SXX} represents the relative amplitude of XX component scattered waves.

The variation of $RA_{\rm SXX}$ and $RA_{\rm SYY}$ as a function of fracture dip angle is plotted in Fig. 14. For the 4.92 m source receiver spacing (Fig. 14(a)), the relative amplitude $RA_{\rm SYY}$ is always higher than $RA_{\rm SXX}$. When the fracture dip angle is less than or equal to 20°, the received signal is mainly reflected wave, $RA_{\rm SYY}$ is much larger than

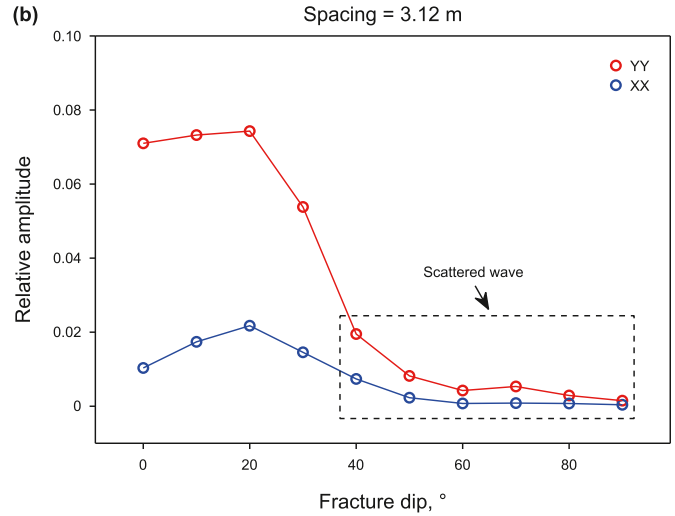


Fig. 14. Relative amplitude of scattered waves under fractures with different dip angles. The red and blue lines stand for RA_{SYY} and RA_{SXX}, respectively. (a) The source receiver spacing is 4.92 m; (b) the source receiver spacing is 3.12 m.

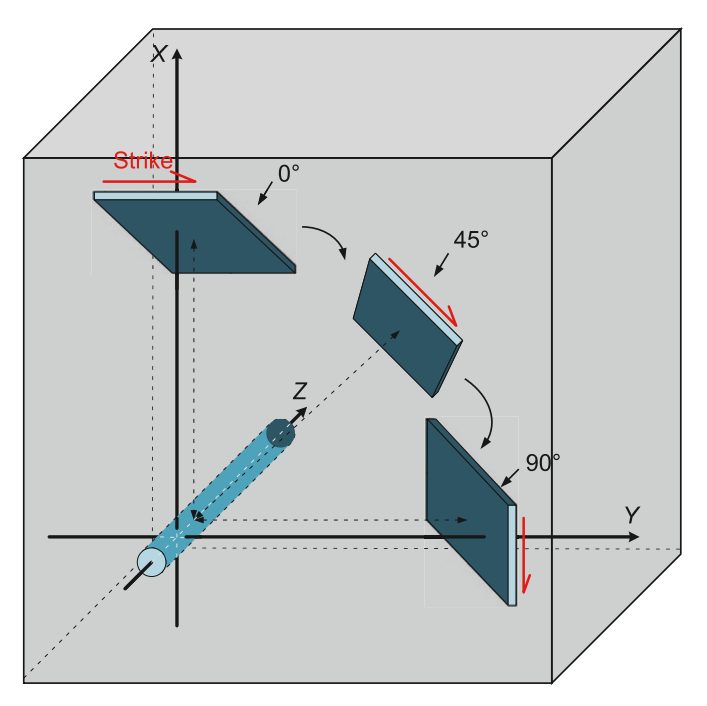


Fig. 16. Schematic diagram of a rock formation model containing fractures having different azimuths with the borehole.

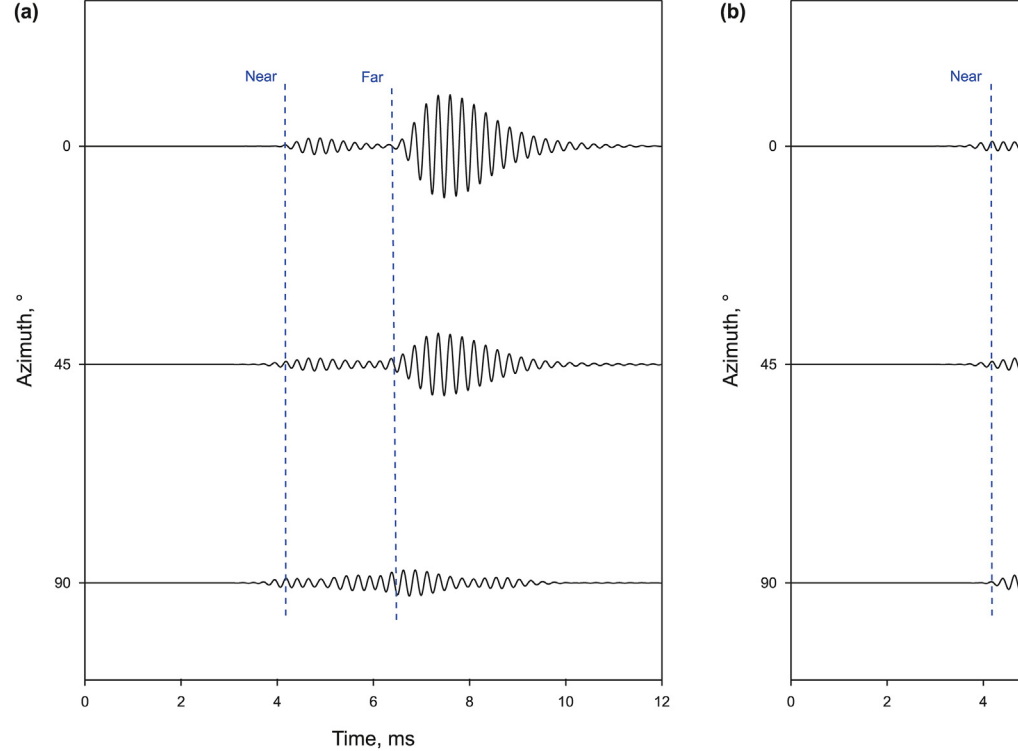
 $RA_{\rm SXX}$. When the dip angle is larger than 20° , the fracture scattered waves dominate in the waveform, $RA_{\rm SYY}$ is slightly higher than $RA_{\rm SXX}$. Interestingly, $RA_{\rm SYY}$ reaches its lowest value at 70° fracture dip angle. The reason is that the receiver is located on the extension

line of the fracture (the red dotted line in Fig. 15), and the scattered waves of both sides of the fracture are eliminated by the interference effect (the area between the two white dotted lines in Fig. 15). As a consequence, the energy of the sound field approaches zero. For the 3.12 m source receiver spacing (Fig. 14(b)), $RA_{\rm SYY}$ is also higher than $RA_{\rm SXX}$. For the fracture dip angle over 20°, the difference between $RA_{\rm SYY}$ and $RA_{\rm SXX}$ is even larger compared with the results in Fig. 14(a). Consequently, we should pay more attention to identify YY component fracture scattered waves with shorter source receiver spacing.

5. Fracture azimuth effect for the scattered wave

We define the azimuth of the fracture as 0° when the fracture center is in the XOZ plane with positive direction of the X axis (see Fig. 16). When the fracture rotates clockwise around the Z axis, different fracture azimuths can be obtained. The fracture parameters remain the same as described in Section 2.2. It should be noted that the dip angle between the fracture and the borehole is fixed at 60° .

The waveforms excited by a horizontally polarized source and received by a horizontally polarized receiver, under different fracture azimuth, are plotted in Fig. 17(a). The direct wave is also removed here. When the fracture azimuth is 0° , the polarization direction of the source is parallel to the strike of the fracture. The SH scattered wave splits into two wave packets with different arrival time. The far-end scattered wave has a stronger amplitude than the near-end, which is consistent with the results in Fig. 5. When the fracture azimuth goes to 45° , the amplitude of the far-end scattered wave becomes weaker. The arrival time of the near-end scattered wave is earlier than that of the 0° azimuth. The reason is that the polarization direction of the source is no longer parallel to the strike



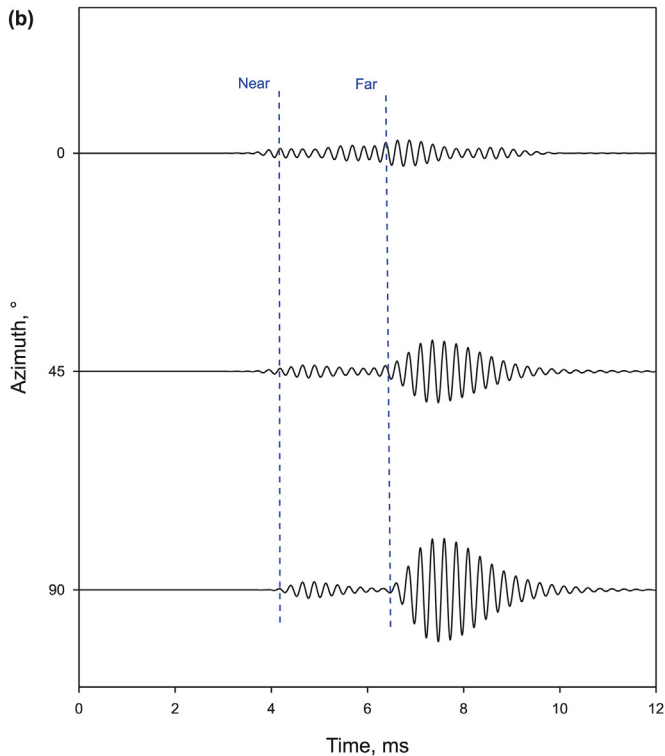


Fig. 17. The received waveforms from fractures with different azimuths. (a) Horizontally polarized source excitation, horizontally polarized receiver receiving waveform; (b) vertically polarized source excitation, vertically polarized receiver receiving waveform.

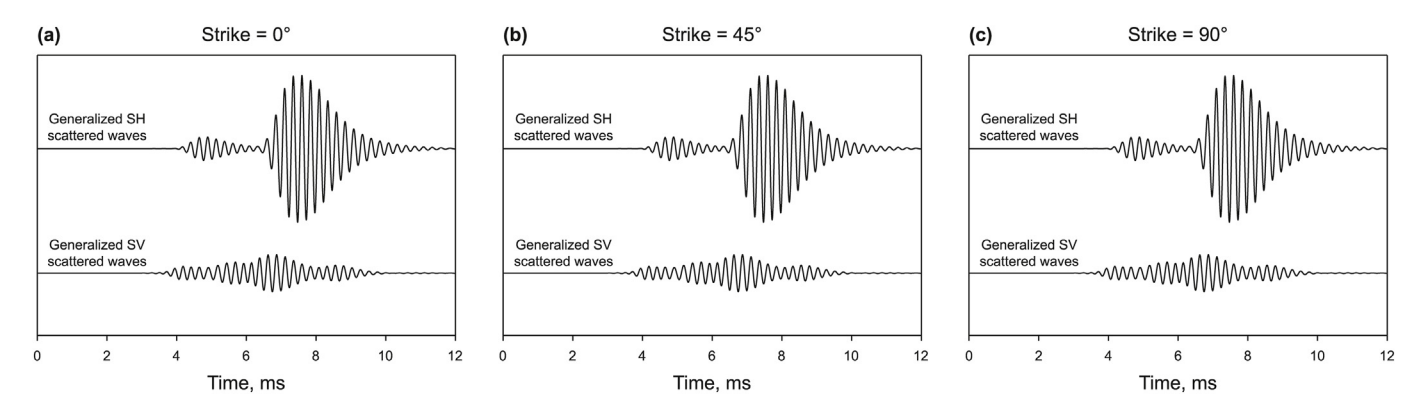


Fig. 18. Generalized SH and SV scattered waves from fractures with different azimuths. (a) Fracture strike with 0°; (b) fracture strike with 45°; (c) fracture strike with 90°.

of the fracture, and scattered wave mode conversion occurs at the near-end of the fracture. Not only the scattered SH-SH wave, but the scattered SH-P wave with faster speed is generated. When the fracture azimuth is 90° , the polarization direction of the source is perpendicular to the strike of the fracture. The amplitude of the farend scattered wave is further reduced, and the wave splitting phenomenon is difficult to be observed.

As the formation is isotropic, the waveforms excited by a vertically polarized source and received by a vertically polarized receiver are consistent with the waveforms excited and received by the horizontally polarized source and receiver, when the fracture azimuth varies reversely (see Fig. 17(b)). For example, the SV-SV waveforms under 90° fracture azimuth are identical to the SH-SH waveforms under 0° fracture azimuth. Considering the effect of borehole orientations, we propose the concepts of the "generalized SH wave" and "generalized SV wave". When the polarization direction of the source is parallel to the strike of the fracture, the reflected or scattered S-wave is called the "generalized SH wave". When the polarization direction of the source is perpendicular to the strike of the fracture, the reflected or scattered S-wave is called the "generalized SV wave".

To further illustrate the characteristics of generalized SH and SV scattered waves, in addition to 0° (Fig. 18(a)) and 90° (Fig. 18(c)) fracture strike, a model with 45° fracture strike is numerically simulated (Fig. 18(b)). It is worth noting that the dipole source corresponding to this model has been rotated by 45° around the Z axis, ensuring the acquisition of generalized SH scattered waves and generalized SV scattered waves (Fig. 18(b)). As can be seen from Fig. 18, the generalized SH scattered waves and generalized SV scattered waves among these three models are completely consistent, which also proves the rationality of the concept of "generalized". As long as the polarization direction of the sound source is parallel to the fracture strike, the corresponding generalized SH scattered waves will possess all the characteristics of the SH scattered waves introduced in Section 4. Similarly, as long as the polarization direction of the sound source is perpendicular to the fracture strike, the corresponding generalized SV scattered waves will also follow all the characteristics of the SV scattered waves introduced in Section 4.

6. Field cases

In the previous sections, we discussed and compared the generation mechanism and the characteristics of fracture reflected wave and scattered wave. In this section, we will use the forward

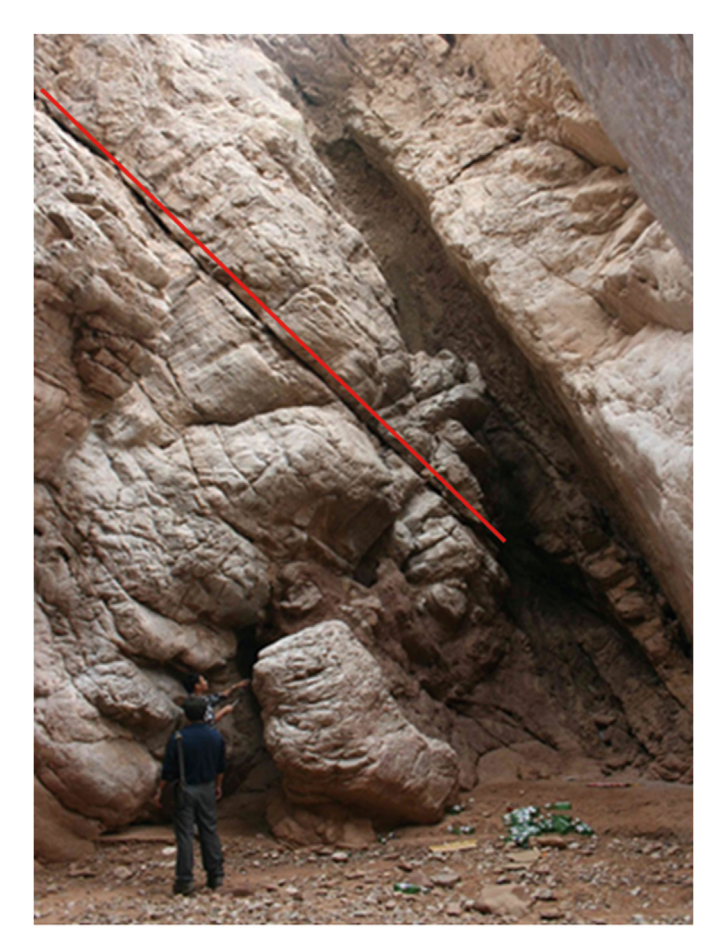
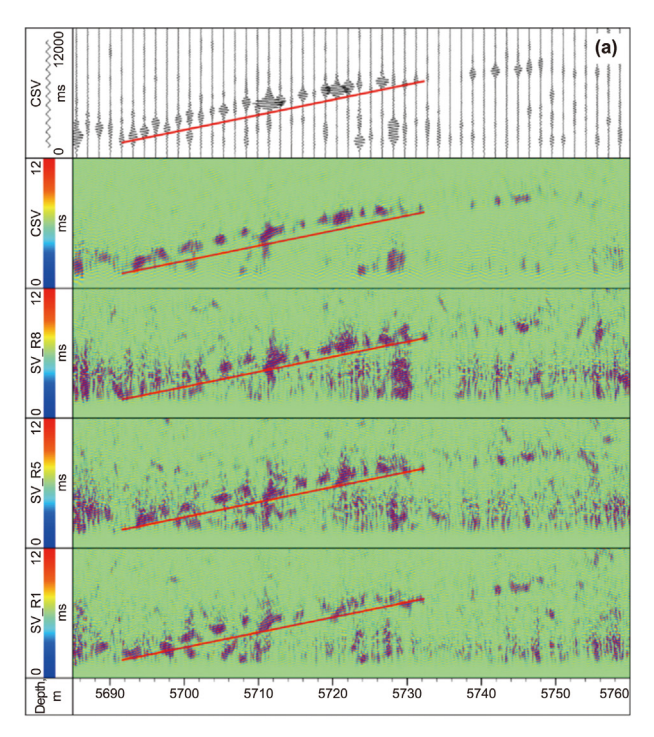


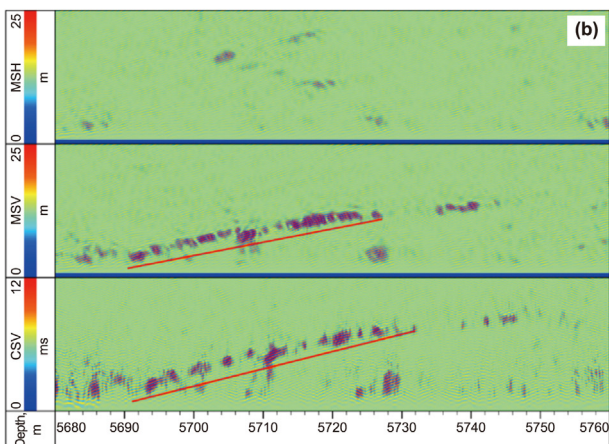
Fig. 19. Fracture in the field outcrop of tight carbonate rocks, and the extension length of the fracture is more than 10 m.

simulation results to explain the reflection and scattering phenomena in two field examples.

6.1. Example of reflected wave from fracture with long length

The first example is from the Tarim Basin, which is a composite basin consisting of the Cenozoic foreland basin and the Paleozoic—Mesozoic craton basin, with an area of approximately





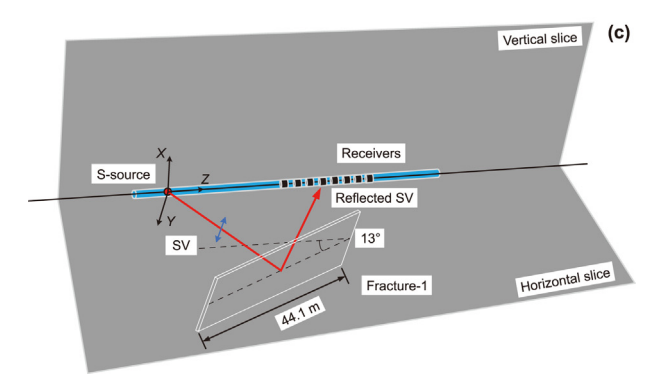


Fig. 20. Measurement and processing results of acoustic logging data for fractures with long length near X1 horizontal borehole in tight carbonate rocks. (a) Reflected waves of the fracture; (b) migration imaging of the fracture; (c) schematic diagram of the structure.

 $56 \times 10^4 \text{ km}^2$. On the metamorphic basement of the Pre-Nanhua system, the thick Nanhua to Quaternary sedimentary rock series develop, where the lithology of the Cambrian-Ordovician strata is predominantly marine carbonate rocks (Yang et al., 2022). Within this stratigraphic sequence, north-northeast and north-northwest trending strike-slip faults develop under the influence of regional stress fields. Based on the scale of the faults, they can be classified as type I, II, and III faults (Wu et al., 2021). Type I fault has a scale exceeding 80 km, type II fault has a scale ranging from 30 km to 80 km, and type III fault has a scale below 30 km. In this region, the development of fractures is closely related to the faults, and the orientation of fractures is also controlled by the regional stress field, typically aligning with the direction of the maximum horizontal stress. A large-sized fracture (length above 10 m, width in centimeters) is presented in the field outcrop (Fig. 19).

In this area, the array acoustic logging data collected from a horizontal borehole is processed. The data process procedures include filtering out the borehole mode waves, restoring the true amplitude of the reflected or scattered waves, and suppressing multiples. In this way, the waveforms corresponding to deep underground fractures can be obtained (Fig. 20(a)). The channels from bottom to top are the depth channel, the SV waveform received by receiver No. 1 (smallest spacing 3.1 m), the SV waveform received by receiver No. 5 (spacing 3.7 m), the SV waveform received by receiver No. 8 (spacing 4.2 m), the common midpoint stack waveform CSV (variable density plot), and the CSV displayed as a waveform. The SV waveforms recorded by three receivers (Nos. 1. 5. 8) all exhibit a wave event spanning from 5690 m to 5733 m in depth, and 2 ms-8 ms in time. This wave event represents a fracture with 44.1 m length in the horizontal slice (Fig. 20(c)). Based on formation S-wave velocity (3300 m/s) and fracture size, we can calculate that the dip angle of the fracture is approximately 13° (Fig. 20(c)). On this basis, a common midpoint stack process based on the travel-time and offset relationship of the reflector is implemented for the 8 receiver waveforms, and the variable density results are shown in CSV in Fig. 20(a). The noise signal is effectively suppressed and the signal representing the fracture is significantly enhanced. This phenomenon indicates that the received waveform is mainly the reflected wave of the fracture. That is to say, fractures with small intersection angles to the wellbore and with large scales usually correspond to reflected waves with strong amplitudes, but not scattered waves. The CSV, CSV migration image MSV, and CSH migration image MSH from bottom to top are plotted in Fig. 20(b). The images MSV and MSH represent the reflected wave migration imaging results of horizontal slices and vertical slices, respectively. By comparing the two images of MSV and MSH, we can see that the reflected SV wave of the fracture is very strong, and the reflected SH wave is very weak. There is a distinct difference between these two amplitudes, which is consistent with the forward modeling results of the reflected waves in Fig. 14. The strong reflected SV wave discussed here belongs to the generalized SH wave introduced in Section 5.

6.2. Example of scattered wave from fracture with short length

The Sichuan Basin is a large composite basin consisting of a marine cratonic basin and a continental foreland basin, with an area of approximately 19 \times 10 4 km². It has undergone complex evolutionary processes involving cratonic, foreland, and continental rift basin phases. Organic-rich shale deposits are widely





Fig. 21. Cores drilled in the X2 vertical well in a tight shale reservoir. The cores contain fractures with short length. (a) Fracture filled with fluid; (b) fracture filled with calcite,

distributed in the Cambrian Qiongzhusi Formation, Ordovician Wufeng Formation, and Silurian Longmaxi Formation. In the Luzhou area in the southern part of the Sichuan Basin, the Wufeng-Longmaxi Formation comprises a shale sequence with abundant organic matter and widespread natural fractures (Guo and Zhang, 2014). Field outcrops, drilling core samples, and electrical imaging logging data in the region provide comprehensive observations and comparative results, indicating that the fractures mainly include diagenetic fractures and structural fractures (Cui et al., 2023). Diagenetic fractures are influenced by various geological processes during shale diagenesis and are typically smaller than 0.5 m in scale. Structural fractures are correlated with the presence of faults in the area, manifested as significant development of structural fractures near faults. Structural fractures generally range in scale from 1 m to 10 m, which are the main focus of this study.

Two cores drilled from the X2 vertical well in the region are presented in Fig. 21. The structural fracture is filled with fluid (Fig. 21(a)) and calcite (Fig. 21(b)), respectively. In the same region, the processing results of acoustic log data collected in a horizontal borehole X3 are illustrated in Fig. 22(a). The channels from bottom to top are the depth channel, the SH waveform received by receiver No. 1, the SH waveform received by receiver No. 5, the SH waveform received by receiver No. 8, the common midpoint stack SH waveform, and the SV waveform received by receiver No. 8. Comparing the waveforms in channels 2, 3 and 4, they all have the wave event from 1756 m to 1761.5 m, and 8 ms-10.5 ms. This wave event represents a fracture with 6.3 m length in the vertical slice (Fig. 22(b)). Based on formation S-wave velocity (2500 m/s) and fracture size, we can calculate that the dip angle of the fracture is approximately 30°. On this basis, a common midpoint stack is implemented for the 8 receiver waveforms, and the variable density results are shown in CSH in Fig. 22(a). The amplitude of the waveform does not increase, but disappears. This phenomenon indicates that the received waveform is the scattered wave of the fracture, rather than the reflected wave.

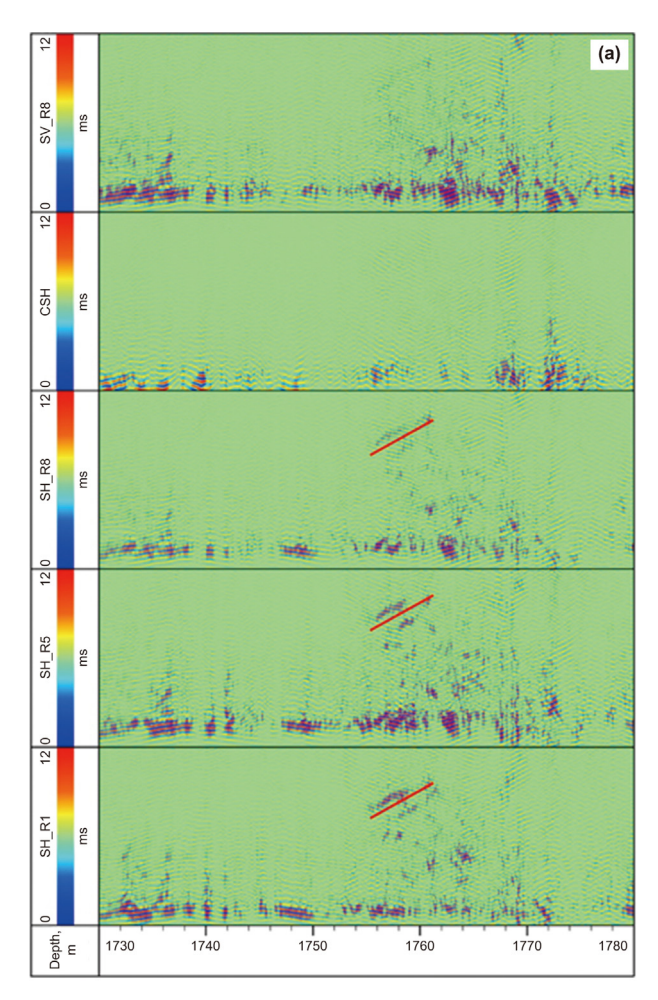
Based on the results of numerical simulation and the field examples, there is indeed a significant difference between the scattered waves and reflected waves. As a consequence, it is infeasible to use reflection wave superposition method to extract scattered

wave signals in the field of inversion. The next crucial task is to effectively utilize the scattered wave forward modeling characteristics studied in this paper, and apply them towards enhancing scattered wave and achieving accurate migration imaging for small-sized scatterers having large dip angles with the borehole.

7. Conclusions

We studied shear waves scattered by short-length fractures (<10 m) with borehole observation system. We established a series of 3D numerical models of rock formation with borehole and short-length fractures. The 3D finite difference algorithm was used for the forward modeling, and the simulated fracture scattered wave field was analyzed. The generation mechanism and characteristics of the fracture scattered wave under the borehole observation system were systematically studied. The work can be concluded as follows:

There is a critical value of the dip angle of the short-length fracture near the borehole, over which the receiver can only receive fracture scattered wave but not the fracture reflected wave. The scattered waves are mainly generated by the two endpoints of the fracture, which forms two different scattered wave packets in the received waveform. When the polarization direction of the acoustic source is parallel to the strike of the fracture, the amplitude of scattered SH-waves is always larger than that of the scattered SV-waves no matter how the fracture dip angle changes. The difference is greater for a logging tool with small spacing (3.12 m) than for large spacing (4.92 m). The SH waves do not perform mode conversion at the fracture endpoints and only the scattered SH waves are generated. The scattered SH waves will travel along the short length fracture and make the fracture itself act as a dipole mode vibration source, resulting in opposite energy polarities of sound waves on both sides of the fracture. We also studied the scattered waves for the fracture having different azimuth with regard to the wellbore. The so called generalized scattered SH wave has the maximum amplitude and the generalized scattered SV wave has the minimum. The field examples also well demonstrate the reflected and scattered waves received by fracture of different scales. This research provides the method for fracture detection and characterization through scattered waves with borehole



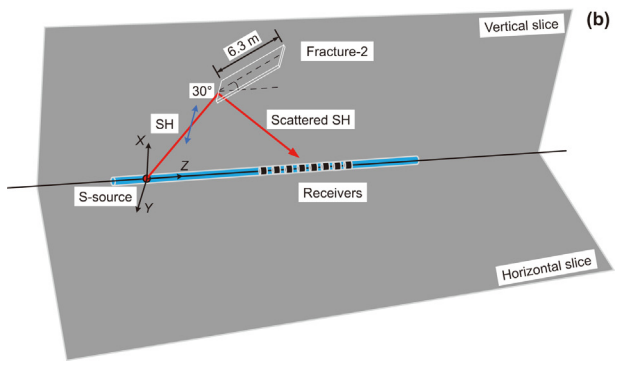


Fig. 22. Measurement and processing results of acoustic logging data for fractures with short length near X3 horizontal borehole in tight shale reservoir. **(a)** Scattered waves of the fracture; **(b)** schematic diagram of the structure.

observation system, and has the potential application in exploring underground fractured rock formations.

CRediT authorship contribution statement

Peng Liu: Writing — review & editing, Writing — original draft, Methodology, Funding acquisition, Formal analysis, Conceptualization. **Hua-Jun Fan:** Writing — review & editing, Writing — original draft, Validation, Methodology, Funding acquisition, Formal analysis, Conceptualization. **Meng-Sheng Zhang:** Writing —

original draft, Visualization, Investigation, Data curation. **Zhen Li:** Visualization, Validation, Investigation. **Jing-Wei Jiang:** Visualization, Data curation. **Yuan Gao:** Validation, Software, Formal analysis. **Ke-Wen Wang:** Writing — original draft, Supervision, Resources, Funding acquisition, Formal analysis, Conceptualization.

Declaration of competing interest

The authors declare that they have no known competing financial interests or personal relationships that could have appeared to influence the work reported in this paper.

Acknowledgments

This work is supported by Scientific Research and Technology Development Project of CNPC (2024ZG38, 2024ZG42), and the CNPC Innovation Fund (2022DQ02-0307).

References

Aki, K., 1969. Analysis of the seismic coda of local earthquakes as scattered waves. J. Geophys. Res. 74 (2), 615–631. https://doi.org/10.1029/JB074i002p00615.

Baird, A.F., Kendall, J.M., Fisher, Q.J., et al., 2017. The role of texture, fractures, and fractures in highly anisotropic shales. J. Geophys. Res. Solid Earth 122 (12), 10341–10351. https://doi.org/10.1002/2017/B014710.

Ben, J.L., Qiao, W.X., Che, X.H., et al., 2020. Field validation of imaging an adjacent borehole using scattered P-waves. Petro. Sci. 17 (5), 1272–1280. https://doi.org/ 10.1007/s12182-020-00475-5.

Blum, T.E., Śnieder, R., Van-Wijk, K., et al., 2011. Theory and laboratory experiments of elastic wave scattering by dry planar fractures. J. Geophys. Res. Solid Earth 116, B08218. https://doi.org/10.1029/2011JB008295.

Burns, D.R., Willis, M.E., Toksöz, M.N., et al., 2007. Fracture properties from seismic scattering. Lead. Edge 26 (9), 1186–1196. https://doi.org/10.1190/1.2780790.

Chen, T.R., Li, J.L., Toksöz, N., 2013. Simulating shear wave propagation in two-dimensional fractured heterogeneous media by coupling boundary element and finite difference methods. Geophys. J. Int. 194 (3), 1810–1822. https://doi.org/10.1093/gji/ggt193.

Chen, X.Y., Zhao, J.Z., Li, Y.M., et al., 2019. Numerical simulation of simultaneous hydraulic fracture growth within a rock layer: Implications for stimulation of low-permeability reservoirs. J. Geophys. Res. Solid Earth 124 (12), 13227–13249. https://doi.org/10.1029/2019JB017942.

Chen, Y.H., Chew, W.C., Liu, Q.H., 1998. A three-dimensional finite difference code for the modeling of sonic logging tools. J. Acoust. Soc. Am. 103 (2), 702–712. https://doi.org/10.1121/1.421230.

Cheng, L., Che, X.H., Qiao, W.X., et al., 2023. 3D trajectory inversion of an adjacent well using scattered P-wave. Petro. Sci. 20, 857–865. https://doi.org/10.1016/ i.petsci.2023.02.024.

Collino, F., Tsogka, C., 2001. Application of the perfectly matched absorbing layer model to the linear elastodynamic problem in anisotropic heterogeneous media. Geophysics 66 (1), 294–307. https://doi.org/10.1190/1.1444908.

Cui, Y., Li, X.Z., Guo, W., et al., 2023. Enlightenment of calcite veins in deep Ordovician Wufeng—Silurian Longmaxi shales fractures to migration and enrichment of shale gas in southern Sichuan Basin, SW China. Pet. Explor. Dev. 50 (6), 1374–1385. https://doi.org/10.1016/S1876-3804(24)60473-8.

Fan, H.J., Liu, P., Zhao, H., et al., 2023. Forward modeling of P- and S-waves response of fractures intersected with horizontal wells in tight reservoirs. Front. Earth Sci. 11, 1149171. https://doi.org/10.3389/feart.2023.1149171.

Fang, X.D., Fehler, M.C., Zhu, Z.Y., et al., 2014. Reservoir fracture characterization from seismic scattered waves. Geophys. J. Int. 196 (1), 481–492. https://doi.org/ 10.1093/gji/ggt381.

Groenenboom, J., Falk, J., 2000. Scattering by hydraulic fractures: finite-difference modeling and laboratory data. Geophysics 65 (2), 612–622. https://doi.org/10.1190/1.1444757

Guo, J.X., Shuai, D., Wei, J.X., et al., 2018. P-wave dispersion and attenuation due to scattering by aligned fluid saturated fractures with finite thickness: theory and experiment. Geophys. J. Int. 215 (3), 2114–2133. https://doi.org/10.1093/gji/

Guo, T.L., Zhang, H.R., 2014. Formation and enrichment mode of Jiaoshiba shale gas field, Sichuan Basin. Pet. Explor. Dev. 41 (1), 31–40. https://doi.org/10.1016/S1876-3804(14)60003-3.

Hei, C., Xiao, Z.B., 2019. Borehole elastic wave anisotropic scattering and application to hydraulic fracturing. J. Petro. Sci. Eng. 183, 106405. https://doi.org/10.1016/ i.petrol.2019.106405.

Leslie, H.D., Randall, C.J., 1992. Multipole sources in boreholes penetrating anisotropic formations: numerical and experimental results. J. Acoust. Soc. Am. 91 (1), 12–27. https://doi.org/10.1121/1.402761.

- Li, D., Tian, X., Hu, H., et al., 2020. Gaussian beam imaging of fractures near the wellbore using sonic logging tools after removing dispersive borehole waves. Geophysics 85 (4), D133—D143. https://doi.org/10.1190/geo2019-0104.1.
- Li, Z., Qi, Q.M., Hei, C., et al., 2022. Elastic-wave radiation, scattering, and reception of a dipole acoustic logging-while-drilling source in unconsolidated formations. Front. Earth Sci. 10, 879345. https://doi.org/10.3389/feart.2022.879345.
- Liu, K.J., Levander, A., 2013. Three-dimensional Kirchhoff-approximate generalized Radon transform imaging using teleseismic P-to-S scattered waves. Geophys. J. Int. 192 (3), 1196–1216. https://doi.org/10.1093/gji/ggs073.

 Liu, P., Qiao, W.X., Che, X.H., et al., 2016. Numerical simulation of azimuthal acoustic
- Liu, P., Qiao, W.X., Che, X.H., et al., 2016. Numerical simulation of azimuthal acoustic logging in a borehole penetrating a rock formation boundary. Geophysics 81 (3), D283—D291. https://doi.org/10.1190/geo2015-0265.1.
- Liu, Q.H., Schoen, E., Daube, F., et al., 1996. A three-dimensional finite difference simulation of sonic logging. J. Acoust. Soc. Am. 100 (1), 72–79. https://doi.org/ 10.1121/1.415869.
- Matsushima, J., Ali, M.Y., Bouchaala, F., 2016. Seismic attenuation estimation from zero-offset VSP data using seismic interferometry. Geophys. J. Int. 204 (2), 1288–1307. https://doi.org/10.1093/gji/ggv522.
- Pan, Y., He, X., Chen, H., et al., 2020. Reflection signals and wellbore scattering waves in acoustic logging while drilling. J. Geophys. Eng. 17 (3), 552–561. https://doi.org/10.1093/ige/gxaa014.
- Shuey, R.T., 1985. A simplification of Zoeppriz equations. Geophysics 50 (4), 609–614. https://doi.org/10.1190/1.1441936.
- Tang, X.M., Patterson, D.J., 2009. Single-well S-wave imaging using multicomponent dipole acoustic-log data. Geophysics 74 (6), 211–223. https://doi.org/10.1190/ 13227150
- Tang, X.M., Wei, Z.T., 2012. Single-well acoustic reflection imaging using far-field radiation characteristics of a borehole dipole source. Chinese J. Geophys-CH. 55 (8), 2798–2807. https://doi.org/10.6038/j.issn.0001-5733.2012.08.031.
- Tang, X.M., Li, Z., Hei, C., et al., 2016. Elastic wave scattering to characterize heterogeneities in the borehole environment. Geophys. J. Int. 205 (1), 594–603.

- https://doi.org/10.1093/gji/ggw037.
- Viswanathan, H.S., Ajo-Franklin, J., Birkholzer, J.T., et al., 2022. From fluid flow to coupled processes in fractured rock: recent advances and new frontiers. Rev. Geophys. 60 (1), e2021RG000744. https://doi.org/10.1029/2021RG000744.
- Wang, T., Tang, X.M., 2003. Finite-difference modeling of elastic wave propagation: a nonsplitting perfectly matched layer approach. Geophysics 68 (5), 1749–1755. https://doi.org/10.1190/1.1620648.
- Willis, M.E., Burns, D.R., Rao, R., et al., 2006. Spatial orientation and distribution of reservoir fractures from scattered seismic energy. Geophysics 71 (5), O43—O51. https://doi.org/10.1190/1.2235977.
- Wu, G.H., Ma, B.S., Han, J.F., et al., 2021. Origin and growth mechanisms of strike-slip faults in the central Tarim cratonic basin, NW China. Pet. Explor. Dev. 48 (3), 595–607. https://doi.org/10.1016/S1876-3804(21)60048-4.
- Wu, R.S., Aki, K., 1985. Scattering characteristics of elastic waves by an elastic heterogeneity. Geophysics 50 (4), 582–595. https://doi.org/10.1190/1.1441934.
- Wu, R.S., Aki, K., 1988. Introduction: seismic wave scattering in three-dimensionally heterogeneous earth. Pure Appl. Geophys. 128 (1/2), 1–6. https://doi.org/ 10.1007/bf01772587.
- Yang, S., Wu, G.H., Zhu, Y.F., et al., 2022. Key oil accumulation periods of ultra-deep fault-controlled oil reservoir in northern Tarim Basin, NW China. Pet. Explor. Dev. 49 (2), 285–299. https://doi.org/10.1016/S1876-3804(22)60024-7.
- Zhang, M.S., Liu, P., Fan, H.J., et al., 2024. Response characteristics of acoustic reflection imaging logging of fractures and formation interfaces outside horizontal wells in tight reservoirs. Chinese J. Geophys-CH. 67 (6), 2439–2454. https://doi.org/10.6038/cjg2024R0399.
- https://doi.org/10.6038/cjg2024R0399.

 Zhao, T., Che, X.H., Qiao, W.X., et al., 2022. Numerical simulation of borehole 3D scanning acoustic imaging using scattered waves. J. Petro. Sci. Eng. 220, 111205. https://doi.org/10.1016/j.petrol.2022.111205.
- Zhu, Z., Burns, D.R., Brown, S., et al., 2015. Laboratory experimental studies of seismic scattering from fractures. Geophys. J. Int. 201 (1), 291–303. https:// doi.org/10.1093/gji/ggu399.